Localization and coalescence of seismicity before large earthquakes

Yehuda Ben-Zion[1] and Ilya Zaliapin[2]

[1]*Department of Earth Sciences and Southern California Earthquake Center, University of Southern California, Los Angeles, CA 90089–0740, USA.*
E-mail: benzion@usc.edu
[2]*Department of Mathematics and Statistics, University of Nevada, Reno, Reno, NV 89557, USA*

SUMMARY

We examine localization processes of low magnitude seismicity in relation to the occurrence of large earthquakes using three complementary analyses: (i) estimated production of rock damage by background events, (ii) evolving occupied fractional area of background seismicity and (iii) progressive coalescence of individual earthquakes into clusters. The different techniques provide information on different time scales and on the spatial extent of weakened damaged regions. Techniques (i) and (ii) use declustered catalogues to avoid the occasional strong fluctuations associated with aftershock sequences, while technique (iii) examines developing clusters in entire catalogue data. We analyse primarily earthquakes around large faults that are locked in the interseismic periods, and examine also as a contrasting example seismicity from the creeping Parkfield section of the San Andreas fault. Results of analysis (i) show that the $M > 7$ Landers 1992, Hector Mine 1999, El Mayor-Cucapah 2010 and Ridgecrest 2019 main shocks in Southern and Baja California were preceded in the previous decades by generation of rock damage around the eventual rupture zones. Analysis (ii) reveals localization (reduced fractional area) 2–3 yr before these main shocks and before the $M > 7$ Düzce 1999 earthquake in Turkey. Results with technique (iii) indicate that individual events tend to coalesce rapidly to clusters in the final 1–2 yr before the main shocks. Corresponding analyses of data from the Parkfield region show opposite delocalization patterns and decreasing clustering before the 2004 M6 earthquake. Continuing studies with these techniques, combined with analysis of geodetic data and insights from laboratory experiments and model simulations, might improve the ability to track preparation processes leading to large earthquakes.

Key words: Earthquake interaction, forecasting, and prediction; Statistical seismology; Dynamics and mechanics of faulting.

1 INTRODUCTION

Laboratory fracturing experiments with heterogeneous materials not dominated by a pre-existing failure surface indicate that large failure events are preceded by a long phase of distributed deformation, followed by a complex progressive localization that culminates with macroscopic instabilities producing the large events (e.g. Lockner *et al.* 1991; Paterson & Wong 2005; Renard *et al.* 2019). Joint analyses of acoustic emission and time-dependent tomography in fracturing experiments document the development of damage zones during the approach to macroscopic instabilities around the eventual system-size ruptures (Stanchits *et al.* 2006; Aben *et al.* 2019). Active crustal regions have heterogeneous fabric and large faults that evolved and localized in earlier deformation phases (e.g. Ben-Zion & Sammis 2003; Schulte-Pelkum *et al.* 2020). However, some large earthquakes occur on faults without clear localized traces before the events, as exemplified by the $M > 7$ (1992 Landers, 1999 Hector Mine, 2019 Ridgecrest) earthquakes that occurred in the

last three decades in the Eastern California shear zone. In addition, laboratory experiments (e.g. Dieterich & Kilgore 1996; Nakatani & Scholz 2004; Johnson & Jia 2005) and *in situ* observations (e.g. Wu *et al.* 2009; Yu *et al.* 2013; Pei *et al.* 2019) indicate that faulted materials have rapid (partial) recovery of properties between failure events that is enhanced with increasing confining pressure (and hence depth).

Creeping fault sections that move more-or-less continuously rather than being locked in long interseismic periods remain localized. However, such fault sections are rare, especially in continental regions where large earthquakes pose significant societal hazard. The progressive recovery of non-creeping seismogenic faults during the interseismic periods implies partial delocalization, which should be correlated with the restrengthening and relocalization before subsequent large earthquakes. Simulations of coupled evolution of earthquakes and faults in a viscoelastic damage rheology model produce localization of deformation before large events and related results consistent with these expectations (e.g. Lyakhovsky *et al.*

1997, 2011). The model results include long interseismic periods with small events that occur in broad zones, localization of deformation leading to large events, and subsequent interseismic periods with partial strength recovery and distributed deformation (e.g. Ben-Zion *et al.* 1999; Ben-Zion & Lyakhovsky 2002; Lyakhovsky & Ben-Zion 2009). Since the duration of large earthquakes is tens of seconds to minutes, while interseismic periods last hundreds to thousands of years (or more), large faults are generally in different phases of interseismic periods during almost all times.

In the last few decades there were several *M* > 7 earthquakes in Southern California (SoCal), but most major faults in SoCal are in interseismic periods and are associated with seismicity (e.g. Hauksson *et al.* 2012; Cheng *et al.* 2018) and geodetic deformation (e.g. Wdowinski *et al.* 2001; Kreemer *et al.* 2014, 2018; Shen *et al.* 2015) in zones that are tens of kilometres wide. During the occurrence of large earthquakes, these deformation regions localize to become large rupture zones with widths that range from submetre (e.g. Chester *et al.* 1993; Rockwell & Ben-Zion 2007) to hundreds of meters (e.g. Johnson *et al.* 1997; Fletcher *et al.* 2014; Milliner *et al.* 2015). Analysis of geodetic and seismic data in the Western United States shows progressive localization of deformation and increasing rate of moderate to large earthquakes in the region (Zeng *et al.* 2018). An improved ability to track the evolving localization of deformation and seismicity might allow monitoring pre-rupture processes and improved forecasting of large earthquakes.

In this paper, we attempt to develop refined techniques for analysing localization of brittle deformation manifested by rock damage production and seismic activity with a focus on the plate-boundary region in SoCal (Fig. 1). We apply these techniques to track and quantify preparation processes leading to large earthquakes using three complementary approaches: (i) Localization of rock damage generated by ongoing background seismicity, (ii) Localization of seismic deformation manifested by evolving fractional area with earthquake activity and (iii) Coalescence of earthquakes into growing clusters. We examine seismic catalogues from SoCal, Parkfield section of the San Andreas fault and region around the 1999 epicentre of the Düzce earthquake in Turkey. The study is part of an effort to improve the understanding of processes leading to large earthquakes and developing robust methods for analysing the dynamics of seismicity.

There is a long history of efforts to forecast large earthquakes with various methods including procedures related to localization of deformation. These include the *M*8 and related algorithms (e.g. Keilis-Borok & Kossobokov 1990; Keilis-Borok & Soloviev 2003), analysis of cumulative Benioff strain (e.g. Bufe & Varnes 1993; Mignan *et al.* 2006), the EEPAS (Every Earthquake a Precursor According to Scale) algorithm (e.g. Rhoades & Evison 2004, 2005) and analyses of related patterns such as the Mogi doughnut (Mogi 1969). These and other algorithms did not lead to significantly improved ability for operational forecasting of large earthquakes, because of the inherent complex dynamics of earthquakes combined with the limited and noisy available data (e.g. Ben-Zion 2008). Procedures that are robust to spatio-temporal fluctuations associated with aftershock sequences, data incompleteness and common catalogue errors are needed to improve the monitoring of approaching large earthquakes. The goals of this study are to develop and implement such procedures.

Ben-Zion & Zaliapin (2019) used basic earthquake scaling relations and fracture mechanics results to estimate the production of cumulative rupture volume (rock damage) by a population of earthquakes. This is done by converting the magnitude of each event to the scalar seismic potency using the empirical scaling relation

of Ross *et al.* (2016), estimating the rupture area of the event assuming a circular crack following the solution of Eshelby (1957) and average strain drop $\Delta\varepsilon = 10^{-4}$, assuming a width that is 1/500 the rupture length based on theoretical and simulation results (Ben-Zion & Ampuero 2009), and summing over the examined event population. Applying the methodology to SoCal indicated that ongoing declustered (background) low magnitude earthquakes generate zones of rock damage that are concentered around the San Jacinto fault zone, the South Central Transverse Ranges, a NW–SE trending zone denoted in Fig. 3 as Eastern SoCal and several other regions. The results also showed that the *M*7.3 1992 Landers and several other moderate earthquakes were preceded by generation of rock damage around their eventual rupture zones. The damage estimates use only low magnitude background seismicity to provide comparative spatial results representing the long-term average interseismic behaviour in all parts the study area.

Fig. 2 extends the space–time domain considered by Ben-Zion & Zaliapin (2019) to include seismicity leading to the 2019 Ridgecrest earthquake sequence in the Eastern California shear zone and to have better coverage around the El Mayor-Cucapah 2010 earthquake in Baja CA. The regions around the rupture zones of the *M*7.1 Ridgecrest and *M*7.2 El Mayor-Cucapah main shocks are seen to have elevated rock damage generated by the ongoing background seismicity in the previous decade or so. The observations suggest that progressive generation of rock damage in connected zones by background seismicity may represent a regional weakening process that allows large ruptures to occur. This is consistent with damage rheology model results, where ongoing events increase the background damage and large earthquakes can occur only when the background damage is high enough over large connected regions (e.g. Lyakhovsky *et al.* 2001; Ben-Zion & Lyakhovsky 2002; Kurzon *et al.* 2019).

In the next two sections we describe the data (Section 2) and methods (Section 3) used in our efforts to quantify evolving localization of seismicity in the crust. The results are described in Section 4 and discussed in Section 5. Most analysed data are associated with earthquakes recorded around large seismogenic faults capable of producing large *M* > 7 events. For context we also examine seismicity from the area around the 2004 *M*6 Parkfield earthquake in the creeping section of the San Andrea fault. The results from the Parkfield area display contrasting tendencies to those associated with the large seismogenic faults.

2 DATA

2.1 Earthquake catalogues

We analyse primarily seismicity of Southern California using the relocated catalogue of Hauksson *et al.* (2012, extended to later years). A version of the catalogue for the time interval 1 January 1981–30 June 2019 used in this study is available at the SCEC data centre https://scedc.caltech.edu/eq-catalogs/. The overall catalogue completeness magnitude is between 2 and 3 (Zaliapin & Ben-Zion 2013) and may differ in space and time depending on the quality of the seismic network. The catalogue includes three *M* ≥ 7 earthquakes (*M*7.3 Landers 1992, *M*7.1 Hector Mine 1999, *M*7.2 El Mayor-Cucapah 2010) and 14 *M* ≥ 6 events. The used catalogue ends five days before the *M*7.1 Ridgecrest earthquake of 5 July 2019 (local time), to focus on the preparation process leading to the event. We also analyse the relocated Northern California catalogue of Waldhauser & Schaff (2008) and Schaff & Waldhauser (2005) that covers the
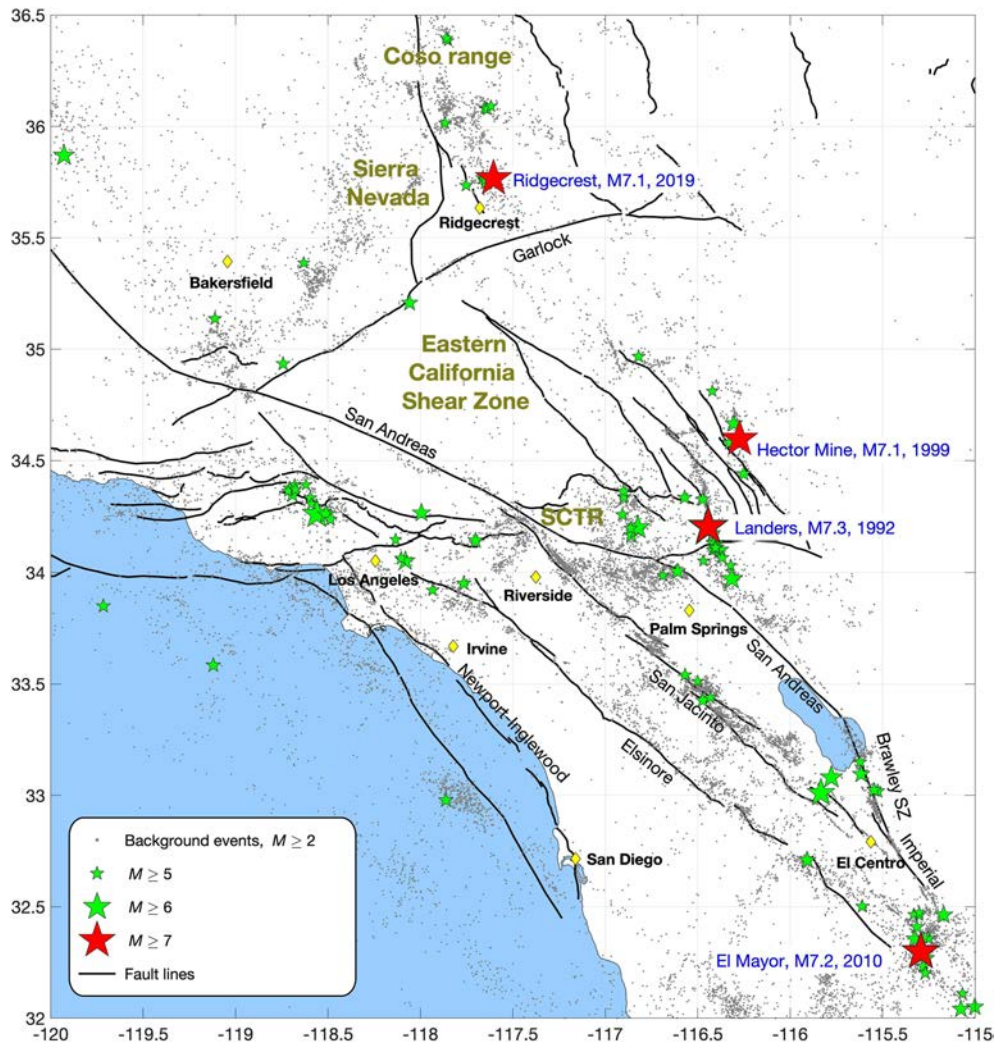
Figure 1. Map of the examined seismicity in Southern California according to the catalogue of Hauksson *et al.* (2012), extended to 2019.5 and declustered according to Zaliapin & Ben-Zion (2020). SCTR stands for South Central Transverse Ranges. See figure legend for other notations.

Parkfield segment of the San Andreas fault, updated for the period 1984–2010. The completeness magnitude in the examined region is about $M_c = 2.5$ and the catalogue includes one moderate event: the $M = 6.0$ Parkfield earthquake of September 28, 2004. Finally, we use a detailed local catalogue of Seeber *et al.* (2000) based on a dense temporary near-fault network to examine seismicity around the epicentre of the 12 November 1999, $M = 7.2$ Düzce earthquake on the North Anatolian fault in Turkey. We consider earthquakes with $M \geq 1.5$ ($M \geq 1.0$ for Düzce) and use epicentre locations since the depth of events is less constrained than the horizontal locations. The earthquakes in the examined catalogues are declustered using the nearest-neighbour methodology of Zaliapin & Ben-Zion (2020).

2.2 Effects of location errors

The average horizontal location error for the estimated background events in the catalogue of Hauksson *et al.* (2012, extended to later years) is 0.48 km, which exceeds almost fivefold the rupture length of an $M_w = 2$ earthquake and is comparable to the rupture length of an $M_w = 3$ earthquake (Ben-Zion 2008). The location errors change systematically in time and space (Zaliapin & Ben-Zion 2015). In

particular, the average location error for background events decreases almost linearly from 0.54 km during 1981–1991 to 0.37 km during 2010–2019, because of corresponding improvements in the density of seismic stations (Fig. S1). Quasi-linear trends of the average location error are also observed in individual regions, each of which is characterized by its own region-dependent average error (Fig. S1).

The time-changing location errors have several effects relevant for the analysis done in this study. Specifically, gradually improving locations may cause artificial localization of the spatial event distribution. Indeed, if the actual spatial distribution of earthquakes remains the same, but location error decrease with time, the event distribution will become progressively a localized version of that at earlier times. This effect is particularly strong if the events are concentrated along low-dimensional structures (e.g. quasi-linear faults), so the proportion of space occupied by events may decrease with time solely because of improved locations. Other localization metrics considered in our analysis (Sect. 3) are also affected by changing location errors. In addition, Zaliapin & Ben-Zion (2015) showed that decreasing location errors produce statistically smaller spatial separation between parent and offspring events. This leads to larger proportion of events that are identified as clustered and
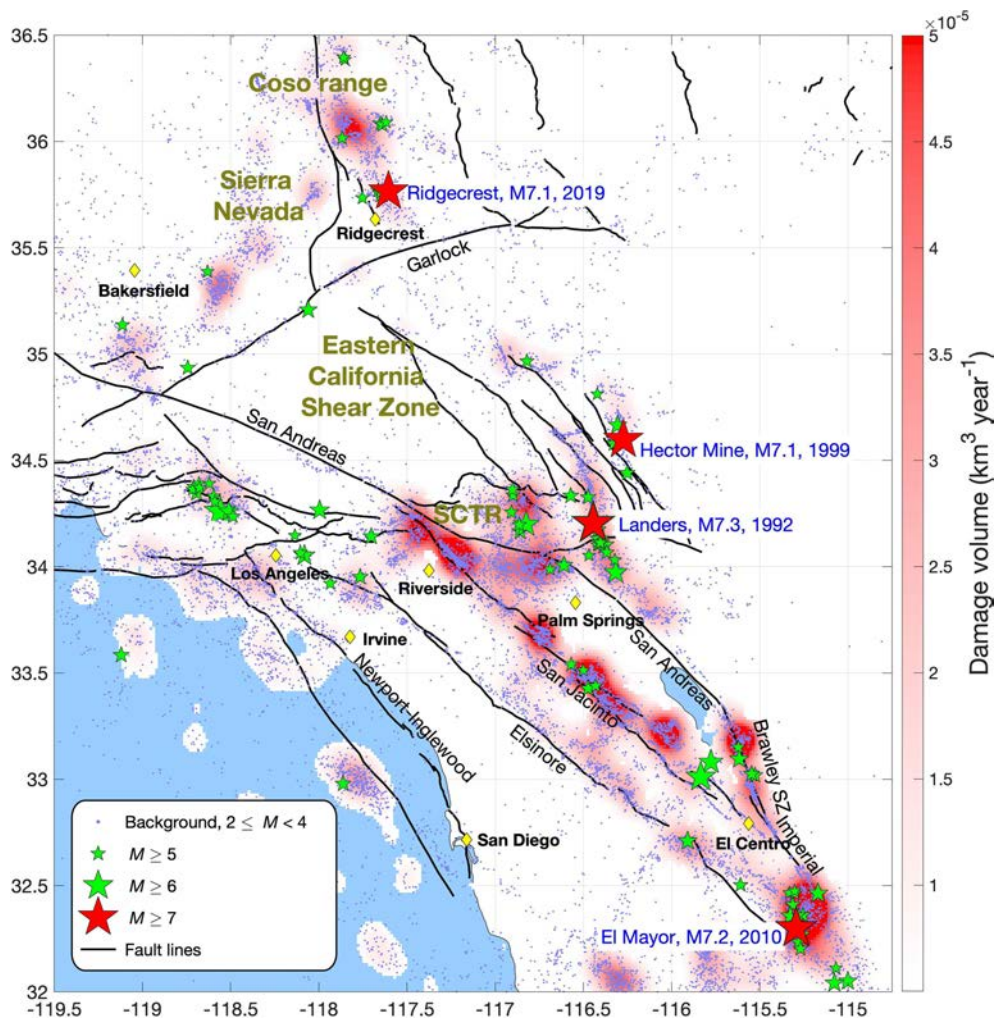
Figure 2. Estimated damage volume V in km^3 yr^{-1} (colour code) projected at the earth surface. The damage is estimated using background events with magnitude $2 \leq M < 4$ during 1981–2019.5 shown by dots. The damage values are clipped at 5×10^{-5} and values below 5×10^{-6} are transparent.

correspondingly smaller proportion of background events. This can affect results discussed in this work based on the estimated background events.

To avoid these artefacts, we focus on local space–time fluctuations of the background events that are not correlated with (or even go against) the decreasing trend of the location errors. For context we also show results associated with long-term changes in the distribution of background seismicity, but emphasize that such results must be critically checked against location error artefacts. The general complexity of the examined phenomena and existence of artefacts related to evolving data quality motivate us to use a set of complementary measures to assess earthquake localization (Section 3). The different measures are applied with a range of parameters and only observations that are suggested robustly by several measures are interpreted as likely reflecting genuine processes.

3 METHODOLOGY

3.1 Absolute and relative localization of measures

We aim to quantify the absolute and relative localization in spatial distributions of background earthquakes as a function of time. Intuitively, *absolute localization* measures the difference between a

given spatial measure and the uniform measure with the same support. The *relative localization* of measure P with respect to measure Q reflects two simultaneous phenomena: (i) measure P is more localized in the absolute sense than Q (i.e. P is further away from the uniform measure than Q), and (ii) both measures concentrate within the same spatial areas.

We analyse localization using the receiver operating characteristic (ROC) framework (e.g. Swets 1973; Molchan & Keilis-Borok 2008; Shcherbakov *et al.* 2010; Jolliffe & Stephenson 2012) formally described and illustrated in Appendix A. Informally, consider a discrete measure P (not necessarily normalized to unity) over a given spatial grid and the uniform measure U with the same support. The ROC curve $R(P|U,P)$ describes the proportion of P (y-axis) contained within a given fraction of most active (i.e. having largest P-weight) spatial cells (x-axis). According to this definition, any ROC curve is contained within the unit square $[0,1] \times [0,1]$. The ROC curve $R(U|U,U)$ for the uniform measure U coincides with the diagonal of this square, and the curve for any non-uniform measure P lies above the diagonal. The Gini coefficient G_P for the measure P equals twice the area between the ROC curve $R(P|U,P)$ and the diagonal line (Breiman *et al.* 1984). The Gini coefficient G_P can take values within the interval $[0,1]$; $G_P = 0$ implies that P coincides with the uniform measure U, and G_P increases toward unity as

P becomes more localized (less uniform). These quantities are discussed further and illustrated in Appendix A1 (Figs A1, A2a, A3a and b). The Gini coefficient is used in Section 4 as a measure of absolute localization of background seismicity (e.g. Figs 7b and 9).

A related quantity $G_{P|Q}$ measures the relative localization of measure P with respect to measure Q. Informally, consider a ROC curve $R(Q|P,Q)$ that describes the proportion of measure Q (y-axis) contained within its most active cells that correspond to a given fraction of P (x-axis). This curve is contained within the square $[0,1] \times [0,1]$ and in general may lie below the diagonal. The coefficient $G_{P|Q}$ is defined as the area above the curve within the square (Appendix A2, Fig. A2b). The coefficient $G_{P|Q}$ can take values within the interval $(0, 1)$. If measures P and Q are concentrated within different regions, then $G_{P|Q} < 1/2$ (Figs A3c and d); $P = Q$ implies $G_{P|Q} = 1/2$, and relative localization of P with respect to Q implies $G_{P|Q} > 1/2$ (Figs A3e and f). The coefficient $G_{P|Q}$ is used in Section 4 as a measure of relative localization of time-conditioned spatial distribution of background seismicity with respect to the time-averaged background distribution.

3.2 Localization of background seismicity

As mentioned, Ben-Zion & Zaliapin (2019) found that several large earthquakes in SoCal are preceded by rock damage generation in volumes around the rupture zones of the future events (Fig. 2). To provide more details on this process, we analyse spatio-temporal variations of declustered (background) earthquakes with a focus on evolving localization of seismicity (and hence rock damage production). Localization corresponds to a decrease in the spatial extent that supports the earthquake-related damage with respect to a long-term distribution, and may be analysed formally with the ROC framework described in Section 3.1.

Specifically, consider a (background) earthquake catalogue

$$C_0 = \{\mathbf{x}_i = (\phi_i, \lambda_i, z_i), t_i, M_i\}, \ i = 1, \ldots, n, \tag{1}$$

where each event is specified by its spatial coordinate $\mathbf{x}_i$, occurrence time t_i and magnitude M_i. Introduce a square spatial grid at the Earth surface with linear latitude cell size $\Delta\phi$. The cells may be indexed by integer pairs (i,j) in the longitude and latitude coordinates, respectively. The long-term space distribution $S = S(i,j)$ of earthquakes is estimated by counting the number of background events that occurred in each cell (i,j) during the entire duration of the examined catalogue. We also consider the time-conditioned space distribution $S(t) = S(t;i,j)$ that only counts background events within the time interval $(t - \Delta t, t]$. Normalizing the measures S and $S(t)$ for each time instant t to have a total count of unity provides results on the relative spatial concentration of events rather than raw numbers.

The degree of absolute events localization at time instant t is estimated using two complementary measures. The first measure is the normalized proportion $P[S(t)]$ of cells with a value of $S(t)$ above a threshold S_0. The threshold is introduced to reduce the influence of spatial cells with spurious low activity; it also reduces the effects of magnitude cut-off selection. The normalization is intended to account for threshold exceedance in time windows of different lengths and is introduced in the following way. Assume that the total duration of the examined catalogue is T yr and the time window used to calculate the time-conditioned space distribution $S(t)$ is Δt yr. Consider the number $N[S,S_0]$ of cells that satisfy the condition $S > S_0$, that is the number of cells such that the total number of events during the examined time interval of duration T in each cell exceeds S_0. Consider also the time series $N[S(t),S_0]$

defined at each examined time instant t as the number of cells that satisfy the condition $S(t) > S_0 \Delta t T^{-1}$, that is the number of cells such that the total number of events during the time interval $(t - \Delta t, t]$ in each cell exceeds $S_0 \Delta t T^{-1}$. We define the normalized proportion as

$$P[S(t)] = N[S(t), S_0] / N[S, S_0]. \tag{2}$$

In case of $S_0 = 0$, we have $P[S(t)] \leq 1$ since only a fraction of active cells (with at least one event during T yr) can be activated within each time window. In case of a small non-zero threshold S_0, the character of $P[S(t)]$ is similar to the case $S_0 = 0$. For sufficiently large thresholds, the picture is more complicated. In an idealized case of constant (in time) earthquake activity within each cell, $P[S(t)] = 1$. In realistic cases, values below unity signify either temporary localization of activity within selected cells, or migration of activity through the examined region (switching of activity among subregions). These two scenarios are easily distinguishable, since in the former case the drop of $P[S(t)]$ below unity is temporary, while in the latter case $P[S(t)]$ stays below unity all the time. Values above unity indicate delocalization (spread) of activity, when selected cells are only active within a limited period of time.

The second measure of the absolute localization is the Gini coefficient $G_{S(t)}$ (Section 3.1, Appendix A1, Fig. A2a) that corresponds to the ROC set $R(S(t)|U,S(t))$. This measure compares the level sets of the time-conditioned measure $S(t)$ with respect to $S(t)$ itself (y-coordinate) and the uniform measure U (x-coordinate). Higher values correspond to higher localization.

The relative localization of the time-conditioned measure $S(t)$ with respect to the time-averaged measure S is quantified with the coefficient $G_{S(t)|S}$ (Section 3.1, Appendix A2, Fig. A2b).

Cells with a small number of events are eliminated before computing the localization coefficients $G_{S(t)}$ and $G_{S(t)|S}$. Formally, we assign zero values to cells that satisfy the condition $S(i,j) \leq S_0$. We also assign zero values to the time-conditioned cells with $S(t;i,j) \leq S_0 \Delta t T^{-1}$. The uniform distribution U used in calculation of the absolute localization is defined as the uniform distribution over all cells such that $S(i,j) > S_0$.

The significance of the results is assessed via reshuffled catalogue analysis. Specifically, for each examined catalogue C_0 we consider a set of N reshuffled catalogues $C_{0,k}$:

$$C_{0,k} = \{\mathbf{x}_{\sigma(i)}, t_i, M_i\}, \ i = 1, \ldots, n, \ k = 1, \ldots, N. \tag{3}$$

Each reshuffled catalogue $C_{0,k}$ preserves the times of events from C_0 and randomly permutes the locations according to a uniform random permutation σ_k on $\{1, \ldots, n\}$. We skip the subindex k on the permutations in the above equation to simplify the notation. The magnitudes are left unchanged in the reshuffled catalogues. The reshuffled catalogues refer to a situation when the spatial distribution of seismicity does not change with time, while preserving the observed fluctuations of the spatial background rates. In the presented results we use $N = 200$. We checked that using any value $N > 100$ leads to results very close to those reported in this work.

3.3 Evolving development of clusters

Formation of earthquake clusters is another important process examined in this work. To quantify earthquake clustering, we use the nearest-neighbour earthquake proximity η introduced and discussed in Baiesi & Paczuski (2004), Zaliapin et al. (2008), Zaliapin & Ben-Zion (2013) and others. The proximity η_{ij} quantifies the space–time separation of a given event j from an earlier event i. It considers

the magnitude M_i of the earlier event to account for the fact that, because of the Gutenberg–Richter statistics, it is more probable to observe a small-magnitude event than a large-magnitude event at the same space–time separation from event j. The definition of the proximity η_{ij} is given in Appendix B.

The cluster analysis is done here using the original catalogues with no declustering. We connect each event j in the examined catalogue to all earlier events with proximities below a threshold value η_0. Such events are called η_0-neighbours of event j. A cluster is defined as an equivalence class with respect to the η_0-neighbour relation. This means that two events belong to the same cluster if there is a path from the later event to the earlier one that consists of η_0-neighbour links. Note that the two events that belong to the same cluster do not have to be η_0-neighbours.

The examined statistic is the average cluster size in a sliding time window. The timing of a cluster is assumed to be that of its first event. We focus on extreme clustering that corresponds to very small values of the threshold η_0, much smaller than those used to separate the background and cluster modes in aftershock cluster studies (e.g. Zaliapin & Ben-Zion 2013, 2020). Accordingly, the duration of detected clusters is short and assigning the cluster time to its first evet does not bias the analysis.

4 RESULTS

4.1 Long-term localization of seismicity in Southern California

We examine evolving localization of background seismicity in So-Cal over an observational period of 38 yr, using (Table 1) a sliding window of $\Delta t = 10$ yr, square spatial cells with $\Delta\phi = 0.1°$ and $S_0 = 0$, and several subregions defined in Fig. 3. As a general reference, Fig. 4 shows the long-term spatial distribution S of background events with magnitude $M \geq 3$ using square spatial cells with $\Delta\phi = 0.5°$ (panel a) and the corresponding ROC set $R(S|U,S)$ (panel b). The Gini coefficient for this distribution is $G_S = 0.82$, indicating a high degree of absolute localization. The ROC set (Fig. 4b) implies that 70 per cent of the background events in the analysed space–time domain are contained within only 10 per cent of the examined cells. This localization is related to the existence of major fault zones, such as the San Jacinto Fault Zone, Eastern California Shear Zone, etc. (Fig. 1). Since this analysis involves declustered seismicity, the discussed localization is not affected by the occasional occurrence of high-intensity and more spatially distributed aftershocks. We note that the absolute values of the Gini coefficient might depend on the used space ($\Delta\phi$) and time (Δt) discretization. However, our focus is on evolving values associated with decrease and increase in time under fixed time and space resolutions.

Fig. 5 shows the proportion $P[S(t)]$ of occupied cells in SoCal and the subregions defined in Fig. 3. The proportion $P[S(t)]$ for the entire SoCal steadily decreases by about 0.1 from about 0.5 in 1991 (the earliest time instant that can be treated with the sliding window of $\Delta t = 10$ yr) to about 0.4 in 2005 (Fig. 5a). The occupied proportion in the reshuffled catalogues also decreases during this period. The general trend reflects an overall real and/or apparent decreasing intensity of the background seismicity. As mentioned in Section 2.2, it is possible that the decreasing $P[S(t)]$ for the entire SoCal may be partially an artefact of progressive improvement in the quality of the derived locations. The proportion $P[S(t)]$ somewhat increases to 0.45 in 2019, as does the proportion in the reshuffled catalogues. Notably, the proportion of occupied cells in the observed

catalogue always stays lower than its counterpart in the reshuffled catalogues; it is also almost always below the respective 95 per cent confidence interval (CI). This suggests that at each examined time interval the seismic activity is concentrated in selected area(s) that have high activity at different times. We illustrate this effect in Section 4.2.

The corresponding evolving absolute localization coefficient $G_{S(t)}$, relative localization coefficient $G_{S(t)|S}$ and ROC sets are shown, respectively, in Figs S2, S3 and S4. The absolute localization $G_{S(t)}$ of the time-conditioned event distribution $S(t)$ increases in the entire SoCal during 1991–2005, with an average value of about 0.72, and then decreases to about 0.71 in 2019 (Fig. S2a). As in the analysis of occupied cells (Fig. 5a), the localization curve for the observed catalogue is always outside the simulated 95 per cent CI. This strengthens the previous suggestion on alternating activation of different areas. The observed increase of the absolute localization is well aligned with the decrease of the proportion $P[S(t)]$ in Fig. 5(a), as expected since both are associated with the same ROC sets $R(S(t)|U,S(t))$. Similar results are seen for the relative localization $G_{S(t)|S}$ of the time-conditioned distribution $S(t)$ with respect to the long-term distribution S for the entire SoCal (Fig. S3a). The increased localization with time is visibly reflected by the evolution of the ROC curves in Fig. S4(a) to more convex curves with transitions from blue (earlier times) to green and red (later times).

Figs 5 and S2–S4 present corresponding results for the following three selected subregions (Fig. 3): Eastern Seismicity Zone in SoCal (panel b), San Jacinto and Elsinore fault zones (panel c), and Mountains and Basins (panel d). The subregion results are consistent with the observations made for the entire SoCal. We observe a steady increase of localization (decrease of the area occupied by background seismicity) during 1991–2005 in Eastern SoCal and San Jacinto & Elsinore zones, and during 1991–2010 in Mountains and Basins. Then the localization trends reverse, increasing to about the initial levels by 2019. The proportion $P[S(t)]$ values (Fig. 5) and absolute localization $G_{S(t)}$ (Fig. S2) in the individual subregions stay within the simulated 95 per cent CI almost all the time, briefly exceeding those during the period of largest localization (approximately 2003–2010). This indicates an absence of substantial switching of seismic activity among parts of these individual subregions. In other words, each subregion behaves generally as a coherent unit. The relative localization $G_{S(t)|S}$ shows more significant variability in Eastern SoCal (Fig. S3b) and Mountains & Basins (Fig. S3d), with a significant upward trend during 1991–2007 and 1991-2010, respectively.

Overall, all three measures of localization show consistent information that is well aligned with the corresponding ROC diagrams. The presented results are stable with respect to (i) alternative versions of stochastic declustering, (ii) parameters Δt ($5 \leq \Delta t \leq 15$) and $\Delta\phi$ ($0.05 \leq \Delta\phi \leq 0.4$) and (iii) examined range of magnitudes ($2 \leq M_{\min} \leq 4.0$). As mentioned, some aspects of these relatively long-term results may be influenced by the improved earthquake locations, but these do not affect changes associated with individual large earthquakes that are the main focus of this study and described in Sections 4.3–4.6. We note that the temporal scale of fluctuations in Fig. 5 is of the same order as the time window ($\Delta t = 10$ yr) used in this analysis. This may suggest the existence of temporal fluctuations over shorter timescale (e.g. $\sim$1–2 yr) of $P[S(t)]$ that are smoothed (time-averaged) by the used window. We focus on detecting such fluctuations in Sections 4.3–4.5 and show that they might be related to the preparation process of large earthquakes. First, however, we discuss below occasional switching of activity between subregions that should be recognized in analyses of data from large space–time domains.

Table 1. Parameters of localization analyses and related figures.

#	Region	Latitude step, $\Delta\phi°$ (total # non-empty cells)	Time window Δt yr	Magnitude range	Threshold S_0	Time interval	Figures
1	Entire Southern California	0.1° (1491)	10	$M \geq 3.0$	0	1981–2019.5 (38.5 yr)	Fig. 5, S2–S4 (panel a)
2	Eastern Southern California	0.1° (188)	10	$M \geq 3.0$	0	1981–2019.5 (38.5 yr)	Fig. 5, S2–S4 (panel b)
3	San Jacinto & Elsinore	0.1° (96)	10	$M \geq 3.0$	0	1981–2019.5 (38.5 yr)	Fig. 5, S2–S4 (panel c)
4	Mountains & Basins	0.1° (137)	10	$M \geq 3.0$	0	1981–2019.5 (38.5 yr)	Fig. 5, S2–S4 (panel d)
5	Eastern Southern California (premonitory)	0.5° (24)	2.5	$M \geq 3.0$	20	1981–2019.5 (38.5 yr)	Fig. 7
6	Landers	0.2° (17)	2	$M \geq 1.5$	30	1981–1992.5 (11.5 yr)	Figs 8–10, S5,S6 (panel a)
7	El Mayor-Cucapah	0.15° (38)	3	$M \geq 1.5$	2	1995.3–2010.3 (15 yr)	Figs 8–10, S5,S6 (panel b)
8	Ridgecrest	0.15° (69)	2	$M \geq 1.5$	40	2004.5–2019.5 (15 yr)	Figs 8–10, S5,S6 (panel c)
9	Parkfield	0.06° (26)	3	$M \geq 1.5$	15	1989.7–2004.7 (15 yr)	Figs 8–10, S5,S6 (panel d)
10	Düzce	0.05° (203)	0.07	$M \geq 1.0$	0	1999.65–1999.86 (0.22 yr)	Figs S7–S9
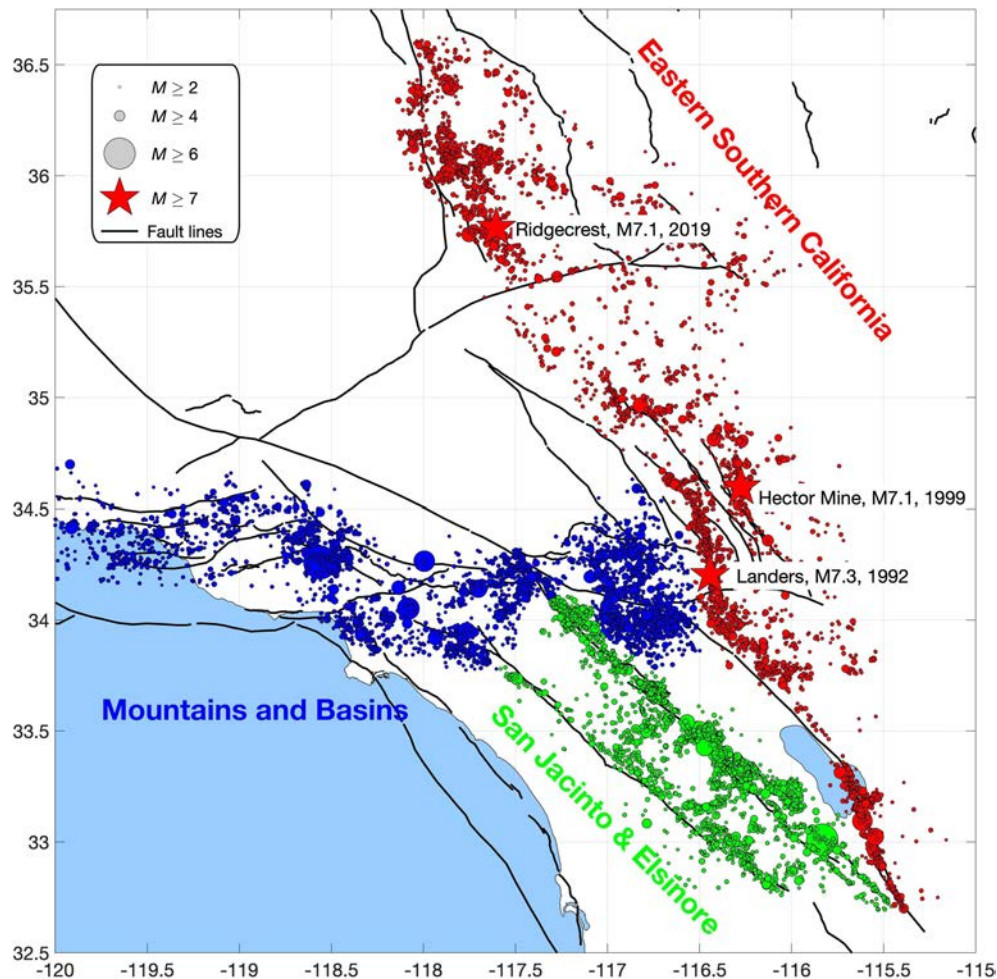
Figure 3. Map of background seismicity in the three selected subregions examined in Sects. 4.1–4.3: Mountains and Basins (blue), San Jacinto and Elsinore fault zones (green) and Eastern Southern California (red). The symbol size is proportional to the event magnitude (see legend). Red stars show three $M > 7$ events.
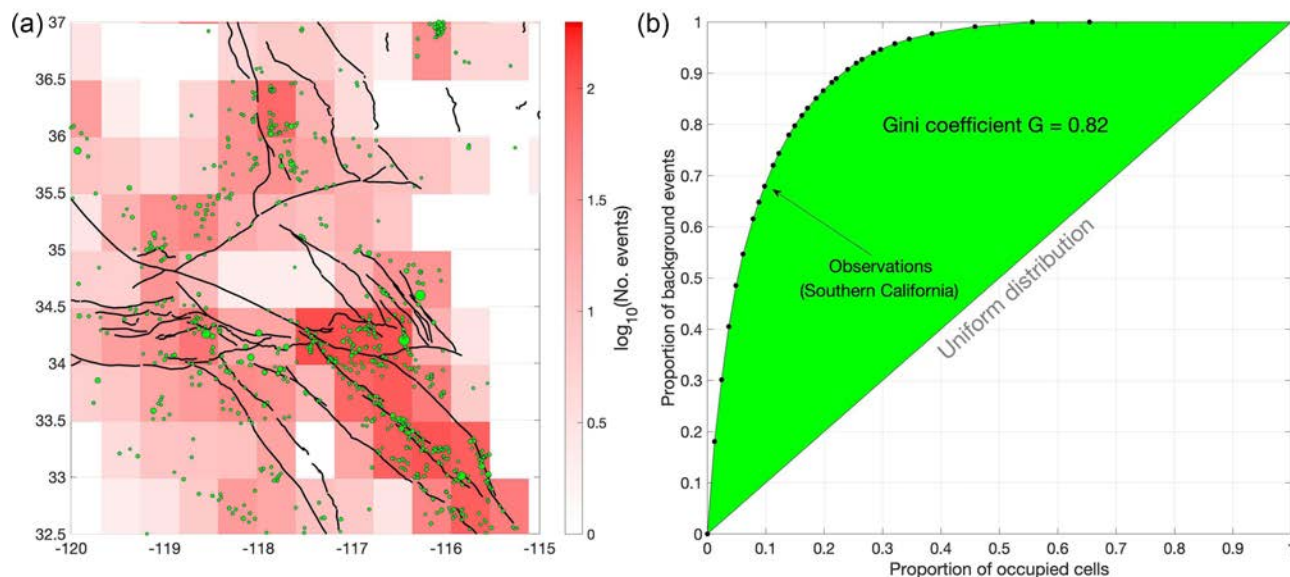
Figure 4. ROC analysis of the background earthquake distribution in SoCal 1981–2019. (a) Number ($\log_{10}$) of background events with $M \geq 3$ (colour scale) in square cells of linear latitude size $\Delta\phi = 0.5°$. Background events with $M \geq 3.5$ are shown by green circles for visual convenience. Black lines show the major faults. (b) ROC diagram $R(S|U,S)$ for the distribution in (a). The *y*-axis indicates the proportion of background events and the *x*-axis shows the proportion of occupied (most active) cells. The inhomogeneity of the spatial background distribution is reflected in deviation of the ROC curve from the diagonal line. The Gini coefficient value is $G_S = 0.82$ (twice the green area).

4.2 Switching of regional seismic activity

As shown in Fig. 5(a), the proportion of spatial cells occupied by background seismicity in a sliding time window in SoCal always stays below the confidence intervals produced by the reshuffled catalogues with fixed space and time marginal distributions taken from the observations. This effect is caused by switching of seismic activity among different subregions. As an intuitive example, consider a union of two regions of equal area, *A* and *B*. Assume that during the first half of the examined time interval only region *A* is active while during the second half only region *B* is active. The proportion of active cells in such a case at any time is $P = 0.5$. However, a reshuffled catalogue with fixed marginal space and time distributions (which are both uniform over the examined space–time region) will have all cells active at any time interval ($P = 1$).

Fig. 6 illustrates the switching phenomenon by showing results for two regions: Eastern SoCal (red) and San Jacinto & Elsinore fault zones (black). Fig. 6(a) displays the number of cells of linear size $\Delta\phi = 0.2°$ that contain more than 3 background events with magnitude $M \geq 3$ in a sliding time window of $\Delta t = 7$ yr. Fig. 6(b) shows the *Z*-score of the damage volume generated by background events with magnitudes $2 \leq M < 4$ in these two regions. The *Z*-score for an array of values *X* is computed as $Z = [X - \text{mean}(X)]/\text{std}(X)$, where mean(*X*) and std(*X*) are the mean and standard deviation of the values, respectively. The number of events and the corresponding damage volume are dominated by the smallest and largest considered earthquakes, respectively. Despite this, and the different magnitude ranges used in these analyses, the results for each region exhibit similar trends. The Eastern SoCal region is more active according to both measures during 2000–2007; while the San Jacinto & Elsinore region is more active during 1991–1996 and 2011–2013. In other words, the activities in the two nearby active regions tend to alternate. The alternating high/low activity in a given region, and related switching of activity among different regions, are general expected behaviour of heterogeneous fault systems (e.g. Dahmen *et al.* 1998; Ben-Zion *et al.* 1999). This is

discussed further in Section 5. The results in Fig. 6(b) suggest that the decadal variation of background activity of the Eastern SoCal region may be a lagged version of that in the San Jacinto & Elsinore fault zone, with a delay of 4–5 yr. Testing this hypothesis requires additional efforts and is deferred to a future work. We now turn to the main focus of this study—evolving localization of seismicity before large earthquakes.

4.3 Premonitory localization of background seismicity in Eastern SoCal

The Eastern seismicity zone of SoCal had the largest ($M \geq 7.0$) earthquakes in SoCal in the examined time interval: 1992 *M* 7.3 Landers, 1999 *M*7.1 Hector Mine and 2019 *M*7.1 Ridgecrest. Another large event in the plate-boundary region is the 2010 *M*7.2 El Mayor-Cucapah earthquake in Baja CA (Fig. 1) that occurred outside Eastern SoCal.

Fig. 7 shows the localization of background seismicity with $M \geq 3$ in Eastern SoCal using a sliding time window of $\Delta t = 2.5$ yr, cells with linear size $\Delta\phi = 0.5°$ and threshold $S_0 = 20$. The occurrence times of the four large events mentioned above are marked by vertical lines. The red lines mark the three large earthquakes that occurred within the examined region and the El Mayor-Cucapah event is marked with blue. Panel a displays the normalized proportion $P[S(t)]$ and panel (b) shows the absolute localization $G_{S(t)}$. There are clear cycles of localization closely corresponding to the occurrence time of the three large earthquakes in the Eastern SoCal region. The normalized proportion $P[S(t)]$ fluctuates about unity during 1984–2019 (Fig. 7a). Notably, it only exhibits substantial decreases (below 0.8 indicated by green dashed line) in the vicinity of the large events: 1–2 yr prior to Landers, Hector Mine and Ridgecrest, and 2–3 yr after El Mayor-Cucapah event. In addition, we observe that a rapid drop of $P[S(t)]$, for over 0.5 units within 2 yr, is only seen within a year before the three largest earthquakes in Eastern SoCal. Similarly, the absolute localization $G_{S(t)}$ (Fig. 7b)
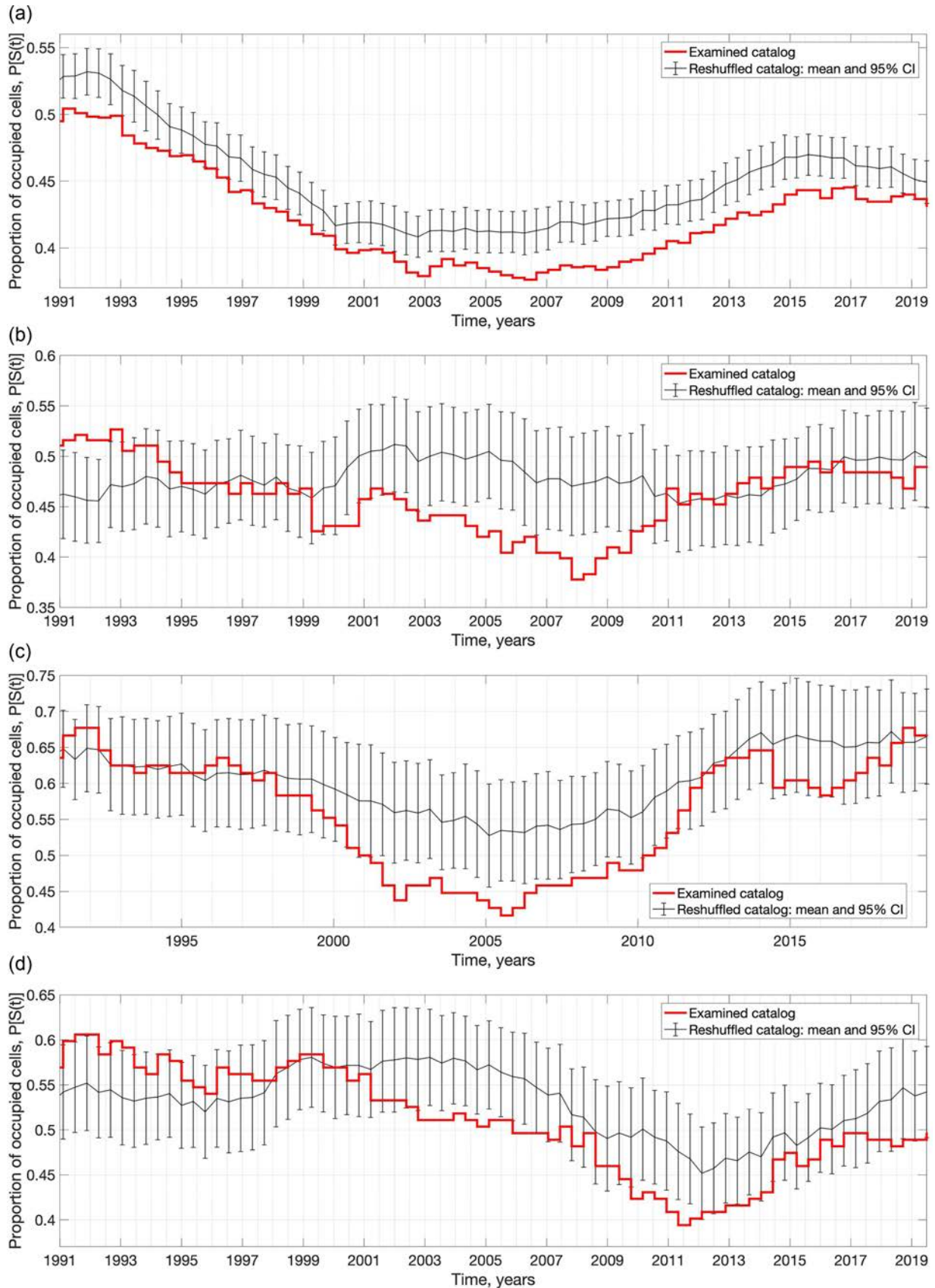
Figure 5. Long-term localization of background events—proportion $P[S(t)]$ of occupied cells in a sliding time window of 10 yr. Red—observations, black—reshuffled catalogues with simulated 95 per cent confidence interval. (a) Entire Southern California. (b) Eastern Southern California. (c) San Jacinto and Elsinore fault zones. (d) Mountains and Basins. The used parameters are in Table 1.
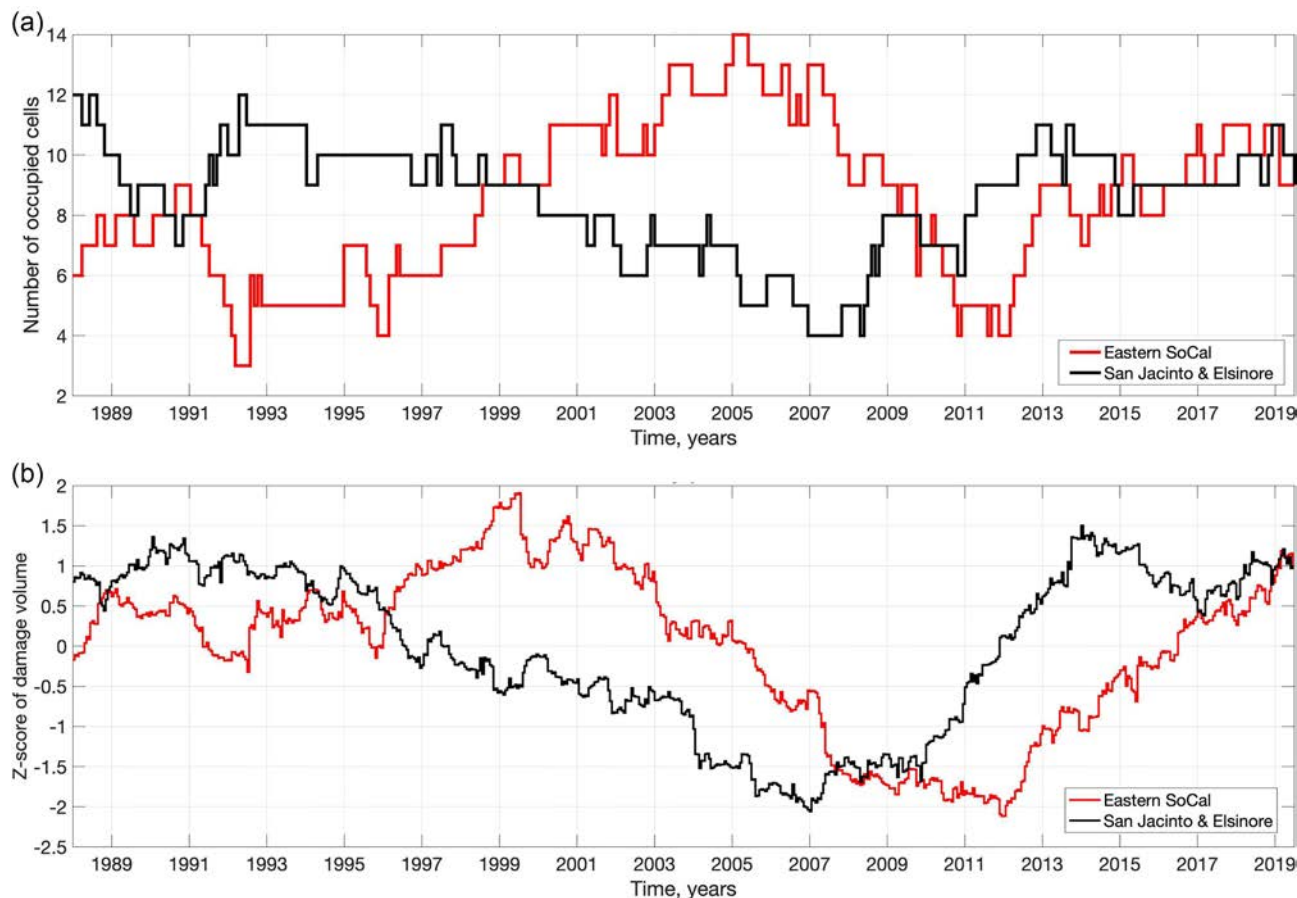
Figure 6. Switching of earthquake activity between the two most seismically active regions in SoCal: Eastern SoCal (red) and San Jacinto & Elsinore fault zones (black). The analysis is done for background events in a sliding time window $\Delta t = 7$ yr. (a) Number of cells with linear size $\Delta \phi = 0.2°$ that contain > 3 events with magnitude $M \geq 3$. (b) Z-score of the damage volume calculated for background events with magnitudes $2 \leq M < 4$.

increases above the level 0.5 (indicated by green dashed line) only in the vicinity of the Landers, Hector Mine and Ridgecrest events, giving no false alarm after El Mayor-Cucapah, and a rapid increase of the localization for over 0.3 units within 2 yr is only seen prior to these three large events.

The discussed results are robust with respect to reasonable variations of parameters associated with sufficient data quality and quantity. To examine further changes associated with large earthquakes, we analyse in the next section data from the space–time vicinity of the events.

4.4 Localization before individual large earthquakes

This section documents several localization processes that occur within the spatial vicinity of large ($M > 7$) main shocks. The examined regions are illustrated in Fig. 8 and are selected based on the rupture zones and aftershocks of the main shocks. Figs 9 and 10 show the absolute localization measure $G_{S(t)}$ and corresponding ROC diagrams for the examined regions. The results illustrated in Fig. 9 for the absolute localization $G_{S(t)}$ are strongly corroborated by those for the normalized proportion $P[S(t)]$ and relative localizations $G_{S(t)|S}$ (Figs S5 and S6). The parameters of the data analyses are listed in Table 1.

Two years prior to the Landers $M7.3$ main shock of 28 June 1992 (Fig. 9a), there is a rapid localization of the background seismicity; $G_{S(t)}$ increases from 0.15 to about 0.5 within 1 yr (late 1990 to

late 1991) and stays at a high level above 0.35 for a year prior to the Landers event. We also note that the values of $G_{S(t)} > 0.4$ are only observed in the examined area within 2 yr prior the Landers main shock, and the only period when the observed values exceed the simulated 95 per cent CI upper limit is within 2 yr prior to the Landers event. A similar pattern is observed around the El Mayor-Cucapah $M7.2$ earthquake of 4 April 2010 in Baja California (Figs 9b, 10b, S5b and S6b). We examine data starting in 1995, 15 yr prior to the event. The absolute localization of $S(t)$ steadily increases from 0.52 to 0.67 during 2005–2009 and exceeds the 95 per cent upper CI within the last 1.5 yr prior to the main shock.

Figs 9(c), 10(c), S5(c) and S6(c) illustrate localization patterns around the Ridgecrest $M7.1$ earthquake of 5 July 2019 (note that the examined catalogue ends 5 d before the event, on 30 June 2019). The analysis is done within the 15 yr interval prior to the main shock. The only time when the absolute localization exceeds the level of 0.7 and is above the upper 95 per cent CI is observed within 1 yr prior to the Ridgecrest event. To have an example from another tectonic domain, we also examine seismicity from the region around the Düzce $M7.2$ earthquake of 12 November 1999 in Turkey. This case study utilizes a detailed catalogue around the space–time domain of the Düzce event, derived from data of local deployment around the eastern end of the rupture zone of the earlier $M7.4$ Izmit earthquake (Seeber *et al.* 2000). The available catalogue covers 0.21 yr prior to the Düzce main shock. During this time, we observe a steady and strong localization with $G_{S(t)}$ increasing from 0.74 to over 0.78
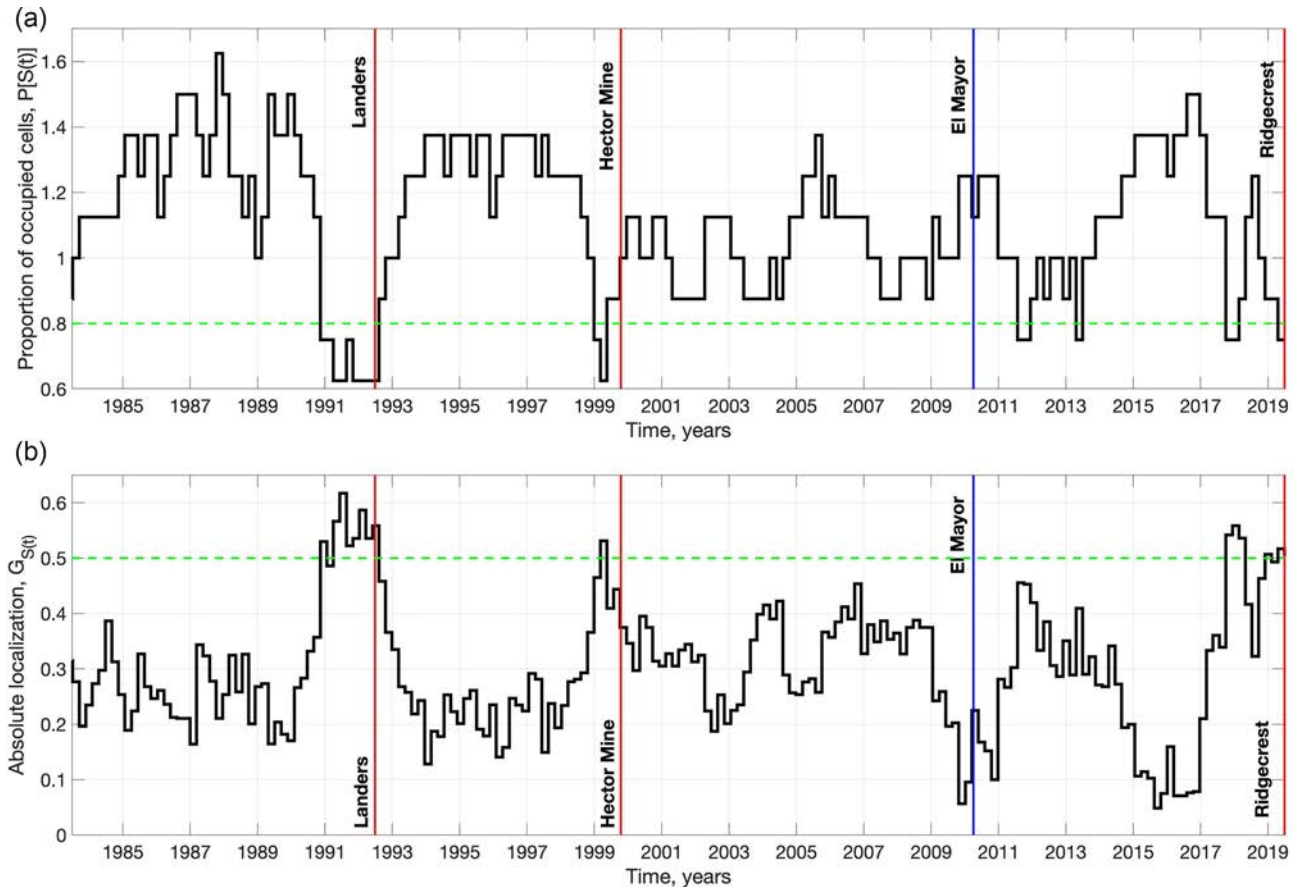
Figure 7. Premonitory localization of background events within Eastern SoCal. The times of the three largest ($M > 7$) earthquakes in the region are shown by vertical red lines. The time of the El Mayor-Cucapah event outside the examined region is shown by the vertical blue line. The analysis uses $M \geq 3$ background events, sliding time window of $\Delta t = 2.5$ yr, spatial cells with $\Delta\phi = 0.5°$, and threshold $S_0 = 20$. (a) Normalized proportion $P[S(t)]$. (b) Absolute localization $G_{S(t)}$. Green horizontal lines emphasize increased (panel a) or decreased (panel b) values of the examined statistic prior to the large earthquakes.

and staying above the upper 95 per cent confidence limit for several days prior to the main shock (Figs S6–S9).

4.5 Delocalization of seismicity before the 2004 M6 Parkfield earthquake

A reversed effect is observed during the time interval leading to the Parkfield M6 earthquake of 28 September 2004, based on data in the relocated catalogue of Waldhauser & Schaff (2008). Figs 9(d), S5(d) and S6(d) display the three localization measures considered in this work for the Parkfield section of the San Andreas fault for the 15 yr prior to the Parkfield earthquake. During this period, each of the three examined measures roughly follows the simulated CI and only exceeds the 95 per cent limits once—a year and a half prior to the M6 event. In the Parkfield area (Fig. 8d), the normalized proportion of occupied cells increases, while the absolute and relative localizations decrease. The respective ROC diagrams are shown in Fig. 10(d). The seismicity along the creeping section of the San Andreas fault is generally highly localized (e.g. Thurber *et al.* 2006). The observed delocalization of seismicity prior to the M6 event may reflect the development of increasing stress level around the Parkfield asperity that produces failures over progressively wider region. This pattern is in marked contrast to the observations around locked fault sections of distributed seismicity that localize toward the rupture zones of main shocks before the events.

4.6 Evolving earthquake clusters before large events

This section documents changes in the size of tight earthquake clusters that occur in the spatial vicinity of large ($M > 7$) main shocks and the M6 Parkfield event in the final year before they occur. The analysis is based on the full (rather than declustered) catalogues and the same spatial regions used in Sections 4.4–4.5 (Fig. 8). We use a small value of the proximity threshold η_0 to focus on highly tight clusters formed by abnormally close groups of events (closer than what would be used for aftershock detection). The parameters of analysis are reported in Table 2.

The available data prior to the 1992 $M7.3$ Landers earthquake span 11.5 yr. In the spatial vicinity of this event, the average cluster size of events with $M \geq 3$ and $\eta_0 = -6$ stays below 2 during 1983–1991, and exhibits a steady increase to above 3 within 2 yr prior to the Landers main shock (Fig. 11a). The only period when the average cluster size stays above 2.5 is in the year prior to the Landers main shock. Before the 1999 M 7.1 Hector Mine earthquake the available data separated from the Landers aftershocks is not sufficient to perform the coalescence analysis.

In the spatial vicinity of the 2010 $M7.2$ El Mayor-Cucapah earthquake, the average cluster size of events with $M \geq 3.5$ and $\eta_0 = -4$ stays below 6 for over two decades during 1984–2008, and then rapidly increases to over 13 1.5 yr prior to the main shock (Fig. 11b). Within the examined interval of 29.3 yr, the only time period when
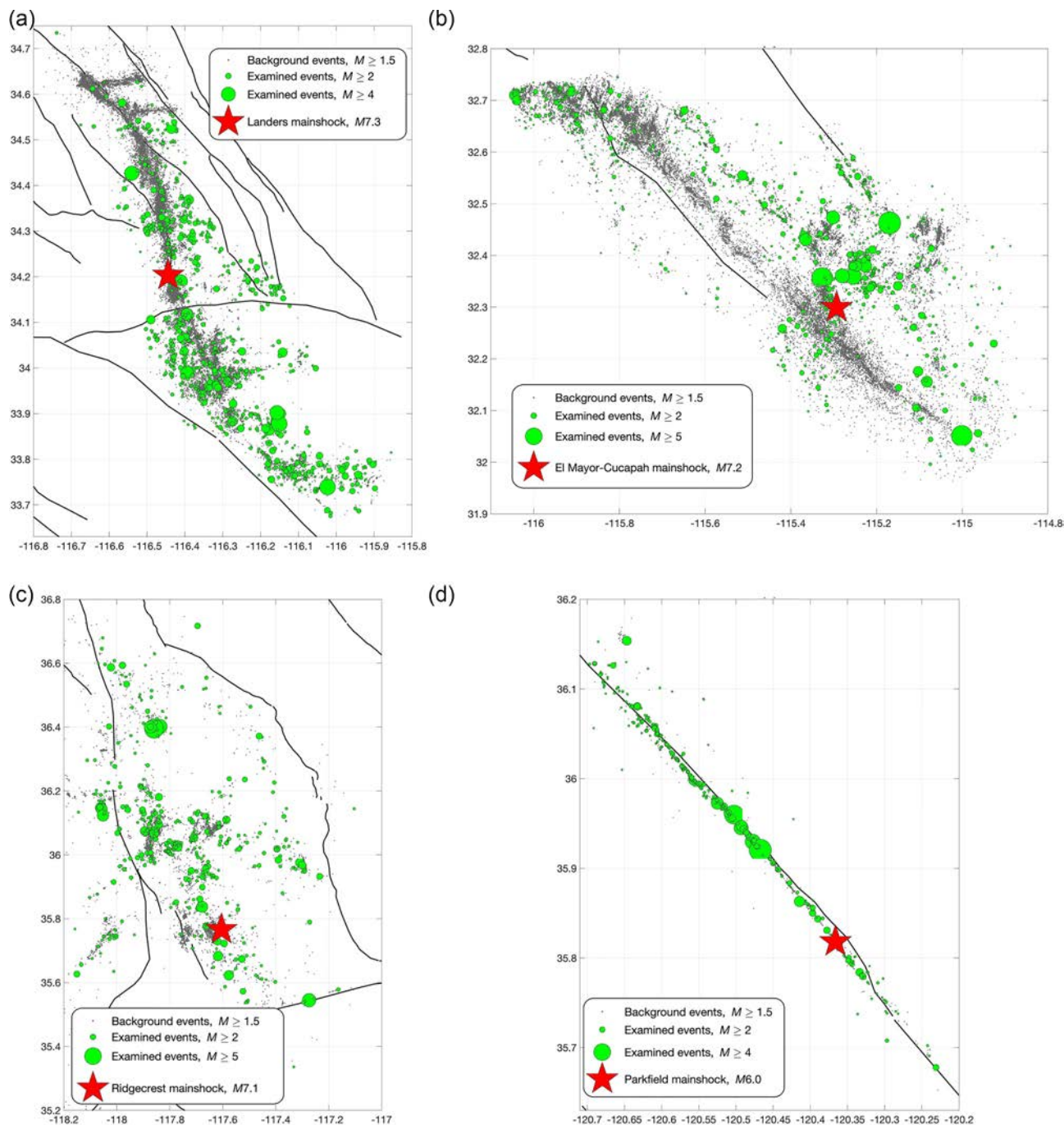
Figure 8. Regions examined for localization of background seismicity before large earthquakes in Figs 9 and 10. (a) Landers, M7.3. (b) El Mayor-Cucapah, M7.2. (c) Ridgecrest, M7.1. (d) Parkfield, M6. The analysis parameters are listed in Table 1.

the average cluster size stays above 6 is within 2 yr prior to the main shock.

In the vicinity of 2019 M7.1 Ridgecrest earthquake, we examine clustering during 19.5 yr prior to the main shock or since 2000. The earlier period is excluded to avoid contamination of results by (i) the aftershocks of Landers event, which triggered significant activity within the Ridgecrest area during 1992 including a series of M4 earthquakes and the associated compound aftershock sequence and (ii) a triplet of M5 earthquakes that occurred between 1995.6 and 1996.1 and triggered strong compound aftershock sequences. The average cluster size of events with $M \geq 1.0$ and $\eta_0 = -8$ stays

below 1.12 during the decade 2004–2013 and steadily increases during 2012–2019 to 1.2 (Fig. 11c). The only time interval when the average cluster size exceeds 1.15 is within 3 yr prior to the Ridgecrest main shock. The low values and small absolute increase in the cluster size in this analysis is related to the very small value of the threshold.

A similar increase of the average cluster size is documented for the 1999 M7.2 Düzce earthquake (Fig. S10). Here, the average cluster size of events with $M \geq 2.0$ and $\eta_0 = -7$ stays below 1.3 since the beginning of the examined catalogue, and rapidly increases to above 2 several days prior to the main shock.
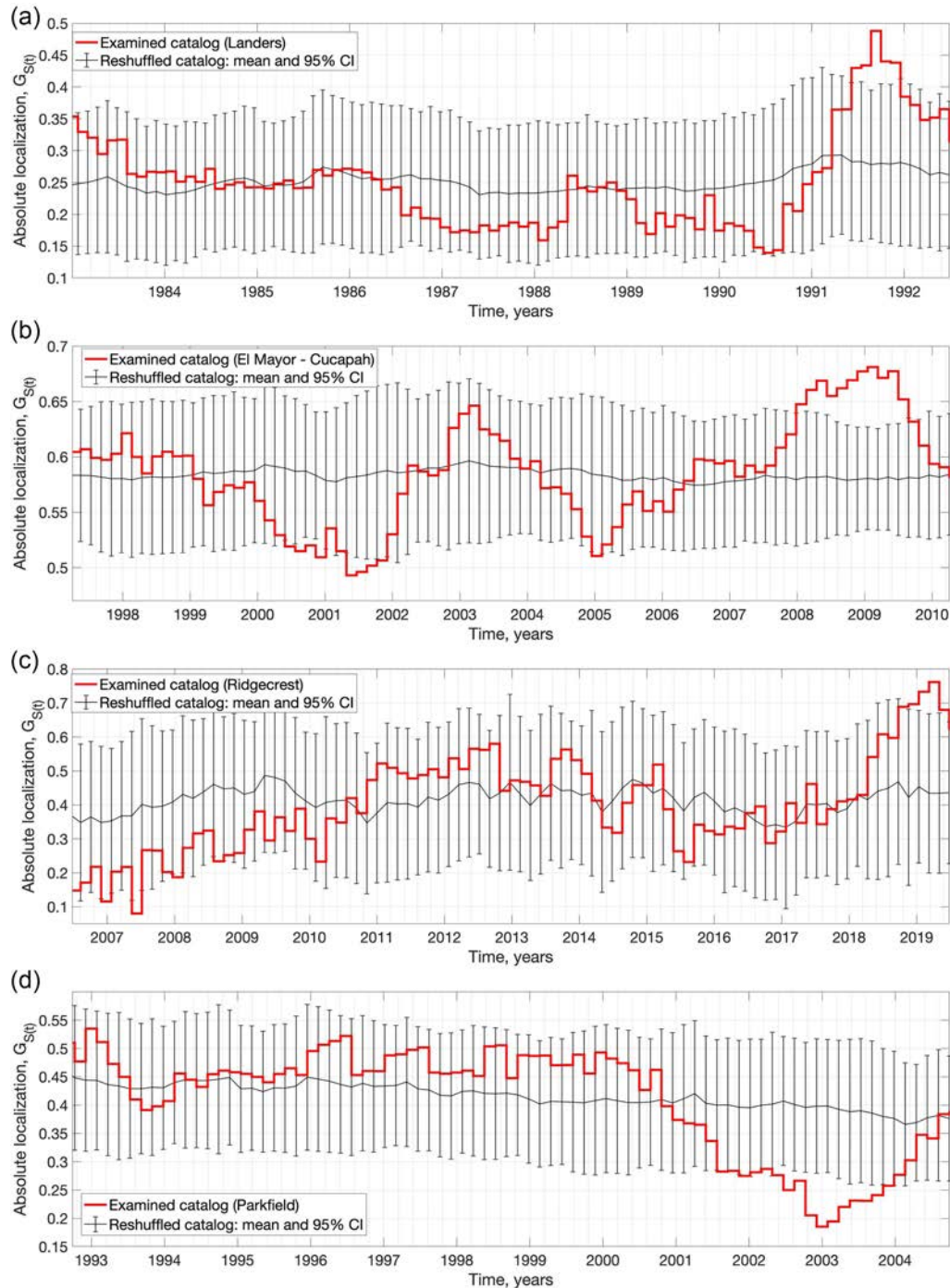
Figure 9. Absolute localization, $G_{S(t)}$, of background events before large earthquakes. Red—observations, black—reshuffled catalogues with simulated 95 per cent confidence interval. (a) Landers, $M7.3$. (b) El Mayor-Cucapah, $M7.2$. (c) Ridgecrest, $M7.1$. (d) Parkfield, $M6$. Note the opposite trend (delocalization) prior to the $M6$ Parkfield event. Table 1 lists the analysis parameters.

In contrast to the above results on generally locked faults, in the vicinity of the 2004 $M6.0$ Parkfield earthquake the average cluster size of events with $M \geq 2.0$ and $\eta_0 = -5$ remains above 1.5 (and most of the time above 2) during 1984–2003, and decreases to 1.25 prior to the main shock (Fig. 11d). In particular, we emphasize the steady, almost linear, decrease of the average cluster size from 3.5 to 1.15 during the decade 1994–2004 prior to the main shock.

5 DISCUSSION

The problem of earthquake prediction is at the core of earthquake science, but has remained unrealizable because of the complex involved (only partially understood) dynamics and limited available data (e.g. Turcotte 1997; Keilis-Borok 2002; Ben-Zion 2008; Jordan *et al.* 2011). In the absence of prediction capability, the seismological community adopted a more limited approach associated with
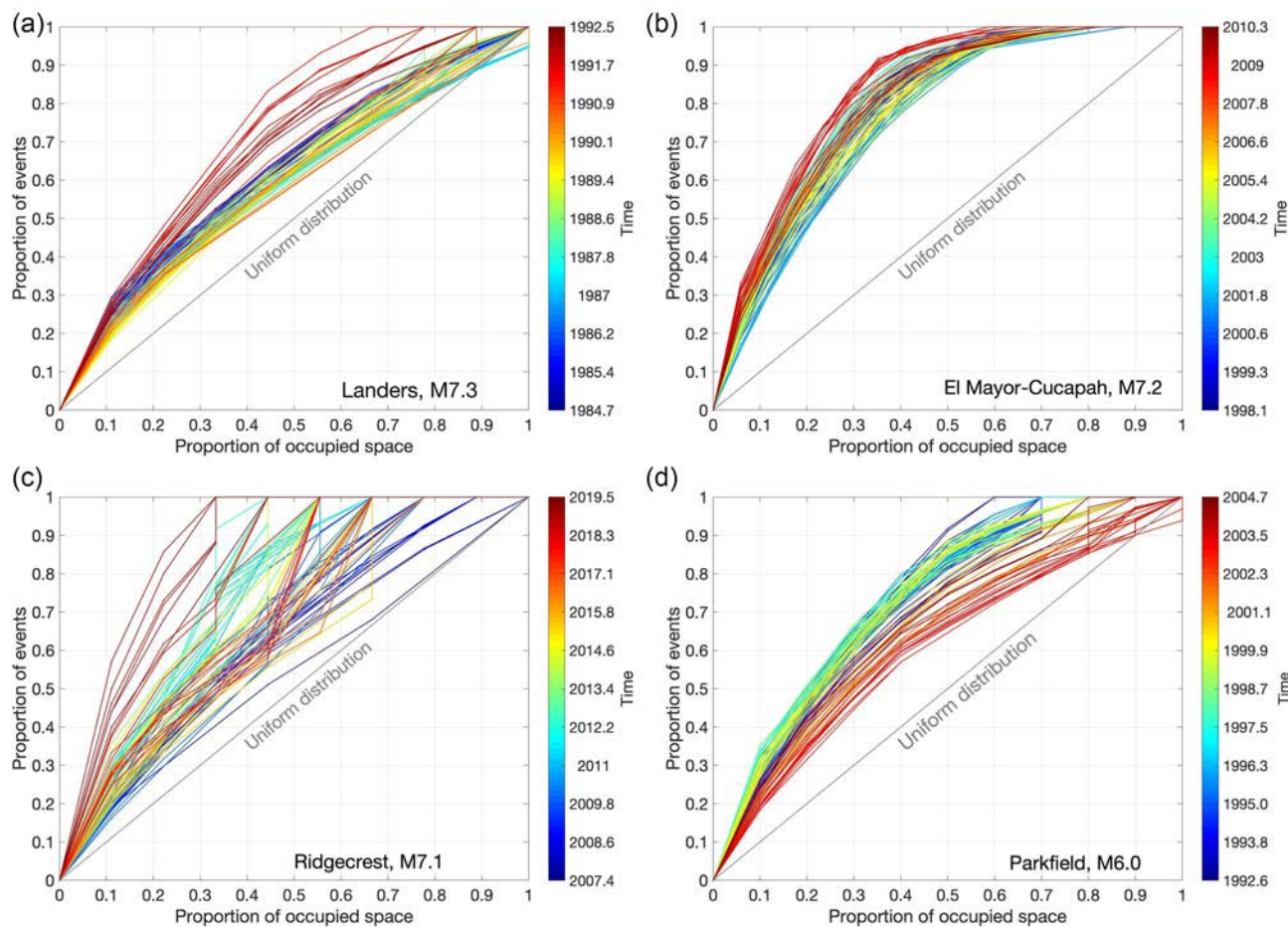
Figure 10. Localization of background events before large earthquakes—ROC set $R(S(t)|U,S(t))$. Different colours correspond to different time windows—from blue to red as time passes (see colourbar). (a) Landers, M7.3. (b) El Mayor-Cucapah, M7.2. (c) Ridgecrest, M7.1. (d) Parkfield, M6.0. In panels (a,b,c) red lines lie further away from the diagonal; this indicates progressive localization. The opposite trend—red lines lie closer to the diagonal—is observed prior to the M6 Parkfield event in panel (c); this indicates delocalization. Table 1 lists the analysis parameters.

Table 2. Parameters of earthquake cluster analyses and related figures.

Main shock	Proximity parameter, d	Proximity parameter, w	Time window Δt yr	Magnitude range	Threshold η_0	Time interval	Figure
Landers, M7.3	1.6	1.0	2	$M \geq 3.0$	−6	1981–1992.5 (11.5 yr)	Fig. 11a
El Mayor-Cucapah, M7.2			3	$M \geq 3.5$	−4	1981–2010.3 (29.3 yr)	Fig. 11b
Ridgecrest, M7.1			4	$M \geq 1.0$	−8	2000–2019.5 (19.5 yr)	Fig. 11c
Parkfield, M6.0			4	$M \geq 2.0$	−5	1984–2004.7 (20.7 yr)	Fig. 11d
Düzce, M7.2			0.02	$M \geq 2.0$	−7	1999.65–1999.86 (0.22 yr)	Fig. S10

forecasting expected ground motion hazard over given time intervals and locations (e.g. Peterson *et al.* 2014; Field *et al.* 2018). In this paper, we attempt to contribute to both hazard estimations and prediction by using seismicity to map the possible existence of large connected zones of ongoing brittle deformation, not necessarily coinciding with large fault structures at the surface, and to track evolving processes that may precede large earthquakes. This is done by estimating the cumulative rock damage generated by background seismicity using scaling relations from earthquake phenomenology and fracture mechanics (Fig. 2), analysing the evolving fractional area occupied by the background earthquakes with parameters of ROC diagrams (Figs 7, 9, 10, S5 and S6) and examining coalescence of individual events into clusters according to an earthquake

proximity parameter (Fig. 11). The different techniques provide information on different timescales and on the spatial extent of weakened damaged crustal regions. We develop and test the techniques using the detailed relocated southern California seismic catalogue (Hauksson *et al.* 2012) with earthquakes reflecting brittle deformation around faults that are locked in the interseismic periods, augmented by data recorded around the 1999 Düzce earthquake rupture on the North Anatolia fault (Figs S7–S10). To have an example of faulting where deformation remains localized during the entire examined period, we also analyse data from the Parkfield section of the San Andreas fault (Figs 7d, 9d, 10d, S5d and S6d).

The results of the present paper and the earlier study of Ben-Zion & Zaliapin (2019) show that several $M > 7$ earthquakes in Southern
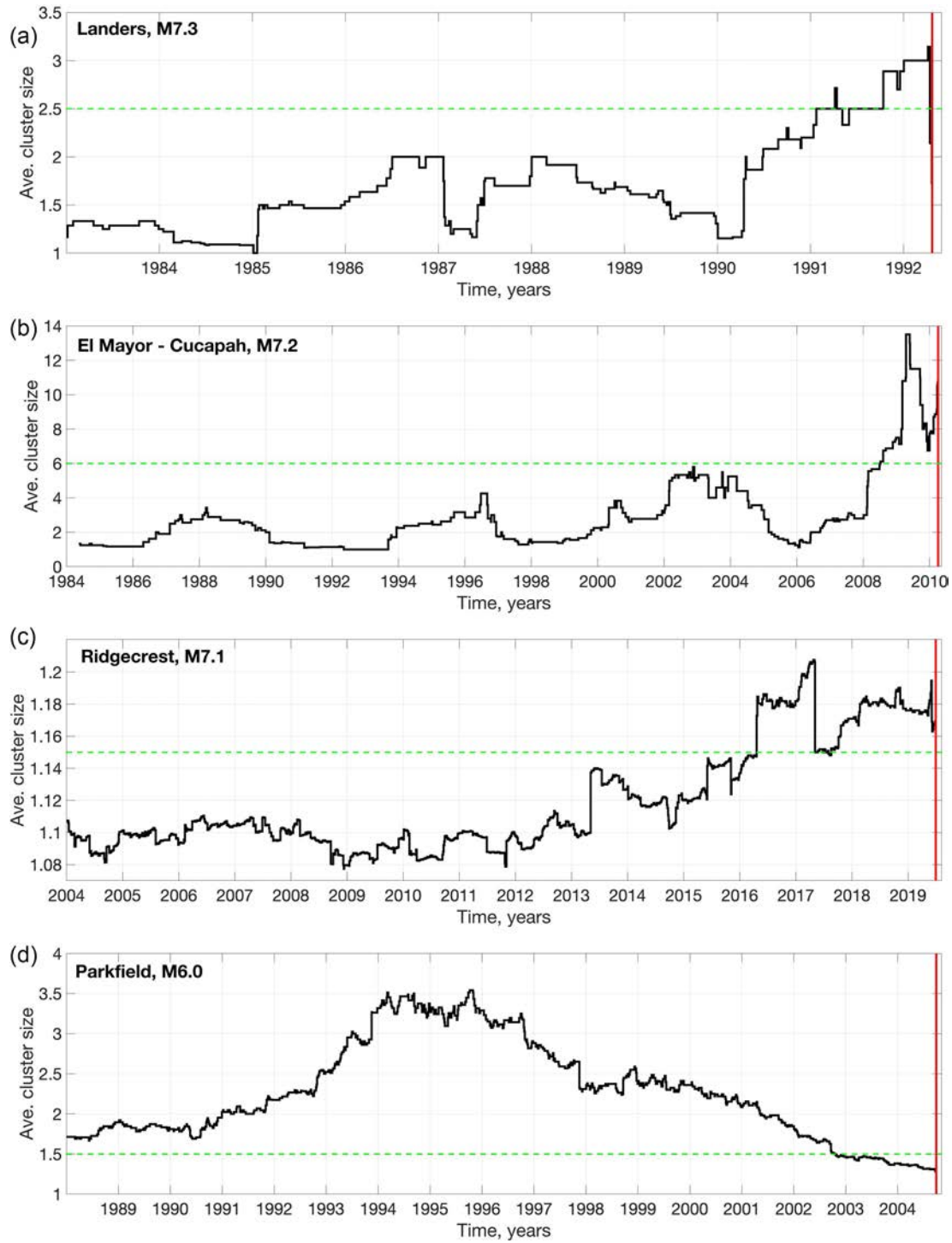
Figure 11. Evolving earthquake clustering before large earthquakes. The black line shows the average cluster size in sliding time windows. The vertical red lines at the right of each panel indicate the time of the main shock. Green horizontal dashed lines emphasize changes of the average cluster size prior to the large events. (a) Landers, *M*7.3. (b) El Mayor-Cucapah, *M*7.2. (c) Ridgecrest, *M*7.1. (d) Parkfield, *M*6.0. Note the opposite trend—decrease of the cluster size—prior to the *M*6 Parkfield event; this indicates delocalization. The analysis parameters of analysis are listed in Table 2.

and Baja California (1992 Landers; 1999 Hector Mine, 2010 El Mayor-Cucapah; 2019 Ridgecrest) were preceded in the previous decades by generation of rock damage around their eventual rupture zones (Fig. 2). The rock damage by the ongoing background seismicity produces a progressive regional weakening, which enables small events to become large ruptures, with main shock size outlined

by the elevated rock damage. Model simulations with a brittle damage rheology indicate that the growth of small instabilities to large events requires the existence of relatively high background damage (e.g. Lyakhovsky *et al.* 2001; Ben-Zion & Lyakhovsky 2006; Kurzon *et al.* 2019). This condition is achieved by the numerus smaller events that generate collectively, during the intervals between large

events, zones of elevated damage that facilitate the occurrence of the large events. A similar process of progressive generation of elevated rock damage before large events is observed in laboratory fracturing experiments (e.g. Lockner *et al.* 1991; Reches & Lockner 1994; Goebel *et al.* 2014; Renard *et al.* 2018; Aben *et al.* 2019; McBeck *et al.* 2019).

Induced seismicity contributes to the rock damage production and is relevant for our results around the Brawley seismic zone and the Coso area. We note that the estimated rock damage in Fig. 2 includes several connected regions with high damage (primarily the San Jacinto fault zone and south central transverse ranges) that can allow propagation of large earthquake ruptures. However, the establishment of such zones provides a necessary but not a sufficient condition for the occurrence of large earthquake. The instabilities producing large earthquakes involve positive feedback between damage-weakening and localization of deformation, and an eventual hypocentre where the stress-strength conditions allow failure to cascade over large-scale damaged region. The final triggering hypocentre at the right place remains essentially a stochastic event.

To provide additional information on the preparation processes leading to large earthquakes we analyse localization of background seismicity into narrower zones by calculating the evolving fractional area in a given region with seismic activity (Appendix A, Figs 5 and S5). We use declustered (background) seismicity to avoid the strong fluctuations associated with aftershocks that can mask more gradual and less pronounced evolutionary processes. Switching of activity among different regions (Fig. 6) adds difficulties to analyses of earthquake processes. This type of behaviour represents a general dynamic regime of seismicity in heterogeneous systems and may be present commonly in earthquake data (e.g. Ben-Zion *et al.* 1999; Lyakhovsky *et al.* 2001; Dolan *et al.* 2007; Rockwell *et al.* 2015). Analysis of low magnitude background earthquakes in Eastern SoCal reveals signatures of progressive localization in data of this entire region 2–3 yr before the $M > 7$ earthquakes in the region (Fig. 7). Analysis of background seismicity in more focused areas around the rupture zones of these $M > 7$ earthquakes, along with those of the 1999 Düzce and 2010 El Mayor-Cucapah main shocks, shows progressive localization ∼2 yr before the events (Figs 9, 10, S5, S6 and S8–S9). In contrast, corresponding analysis for the space–time domain associated with the 2004 M 6 Parkfield earthquake displays (Figs 9d, 10d, S5d and S6d) an opposite delocalization behaviour (background seismicity occupying a broader zone) before the M6 main shock.

The coalescence of individual events into clusters provides information on the final stage of the localization process and is analysed using entire (rather than declustered) catalogues (Figs 11 and S10). The results for regions around the rupture zones of the $M > 7$ earthquakes show that individual events tend to coalesce rapidly to clusters of growing size ∼1 yr before the main shocks. In contrast, corresponding analysis from the Parkfield region indicates decreasing average cluster size before the M6 event (Fig. 11d). We note that the evolving fractional area and coalescence results include the combined effects of multiple foreshock sequences in the examined regions. These analyses can be performed operationally over entire selected regions, in contrast to typical foreshock studies that are done retrospectively around the space–time regions of given main shock hypocentres. An example of such regional analysis is given in Section 4.3, Fig. 7. The statistics used in this work not only show premonitory signals several years prior to the target large events, but also do not produce false signals (false alarms) in the decades before and spatial proximity of the large events (e.g. Figs 9 and 11). These properties are promising for developing further the

used techniques into operational forecasting algorithms. This being said, more work and testing is needed before concluding that the techniques provide robust operational procedures. In particular, it is important to evaluate the rate of false alarms in regional application of the methods and develop uniform (standardized) selection of parameters for analysis in different regions.

The presented results are associated with several types of analyses that have different goals and use different data sets with varying quality and quantity. More specifically (i) the initial analysis of Fig. 5 aims to get a regional background information. This is done by analysing the entire SoCal and each of the three examined subregions with the same sets of parameters (cell size $\Delta\phi = 0.1°$, time window $\Delta t = 10$ yr, magnitude cut-off 3.0, and threshold $S_0 = 0$; Table 1, lines 1–4). As discussed in Section 4.1, varying these parameters within fairly wide ranges does not change the reported aspects of the observations. (ii) The analysis of individual $M > 7$ events (Table 1, lines 6–9) focuses on premonitory localization around impending ruptures. This requires using shorter time windows related to the timescale of the premonitory process (found to be 2–3 yr). To ensure a sufficient number of events in the examined cells, we use lower magnitude cut offs and somewhat larger spatial cells. There is a general consistency among the parameters used in different regions. The same magnitude cutoff $M \geq 1.5$ and time window of 2–3 yr are used in all regions. The spatial resolution used to analyse all events in the SoCal catalogue (Landers, El-Mayor Cucapah, Ridgecrest) is within 0.15–0.2°. The Parkfield section of the San Andreas fault is associated with a well-defined linear zone (Fig. 8d), which is very different from the diffuse seismicity examined in SoCal (Figs 8a–c), so a smaller cell size (0.06°) is used in the Parkfield analysis (Table 1, line 9). The Düzce catalogue covers a very short time interval and smaller spatial domain, which requires its distinct set of parameters (Table 1, line 10). (iii) The intermediate analysis of seismicity in the entire Eastern SoCal (Table 1, line 5) aims to find premonitory signals to multiple $M > 7$ events in data of a single large region (Fig. 3). This is done with the same time window (2.5 yr) as in (ii), related to the timescale of the premonitory process, but larger cell size and larger magnitude cutoff. We believe that the discussed patterns reflect genuine physical processes, and that the results provide a background for continuing research including the development of more general techniques and parameter selection criteria. These will be the subject of follow up studies.

We note that the ROC-based localization statistics used in this paper are closely related to the Shannon information entropy (Shannon 1948) of the background spatial distribution. This can be illustrated as follows. The counts $S(t;i,j)$ of events in spatial cells indexed by pairs (i,j) during the time interval $(t - \Delta t, t]$ are the main objects of our analyses. Let p_i denote the normalized counts (so the total count is unity), indexed arbitrarily over all non-empty examined cells. The corresponding entropy function can be defined as $H(t;S) = -\Sigma \, p_i \ln p_i$. This entropy measure decreases with increasing localization, so the properties of $H(t;S)$ resemble closely those of our localization functions.

The results of the present paper should be augmented by analyses of data from other regions with large active faults and detailed seismic catalogues, such as the San Francisco bay area, Alaska, New Zealand, Turkey and Japan. Analysis of geodetic data can provide important complementary information to the discussed seismic signals by monitoring space–time evolution reflecting both seismic and aseismic deformation in a region (e.g. Craig *et al.* 2017; Socquet *et al.* 2017; Zeng *et al.* 2018). Aseismic signals detected in geodetic data might drive seismic deformation, and can be used to define

space–time regions to monitor for localization of seismicity. Model simulations of localization of deformation in heterogeneous materials (e.g. Finzi *et al.* 2009; Lyakhovsky *et al.* 2011; McBeck *et al.* 2017) and analysis of data recorded in laboratory experiments (e.g. Reches 1988; Lockner & Baylee 1995; Davidsen *et al.* 2017; Zaliapin & Ben-Zion 2018) can help refining expected target signals. Monitoring temporal changes of seismic velocities in fault zones (e.g. Niu *et al.* 2008; Brenguier *et al.* 2019; Baccheschi *et al.* 2020) and evolving susceptibility of fault regions to triggering of seismicity in response to tidal, seasonal and passing seismic waves (e.g. Peng *et al.* 2010; Tanaka 2012; Brinkman *et al.* 2015) can provide additional useful signals on approaching times of large earthquakes.

The coalescence-type representation of seismicity seems to be a promising approach in various earthquake analyses (Zaliapin & Ben-Zion 2018). In this paper, we focused on a simplest coalescence statistic—the number of events in clusters defined by the nearest-neighbour proximity (Section 3.3). Future work can explore more general coalescence structures, represented by time-oriented graphs, whose vertices correspond to individual earthquakes and edges to pairwise proximity between earthquakes. Densifying seismic and geodetic networks in the immediate vicinity of large fault zones can provide additional key information on the final stages of localization and other processes associated with large earthquake ruptures (Ben-Zion 2019). Since reliable forecasting of large earthquakes is unlikely to be operational soon, it is essential to continue to develop improved community preparedness and improved building codes (e.g. Bilham 2009; Detweiler & Wein 2017).

REFERENCES

Aben, F.M., Brantut, N., Mitchell, T.M. & David, E.C., 2019. Rupture energetics in crustal rock from laboratory-scale seismic tomography, *Geophys. Res. Lett.,* **46,** 7337–7344.

Baccheschi, P. *et al.*, 2020. The preparatory phase of the Mw 6.1 2009 L'Aquila (Italy) normal faulting earthquake traced by foreshock time-lapse tomography, *Geology,* **48,** 49–55.

Baiesi, M. & Paczuski, M., 2004. Scale-free networks of earthquakes and aftershocks, *Phys. Rev. E,* **69**(6), 066106.

Ben-Zion, Y., 2008. Collective behavior of earthquakes and faults: continuum-discrete transitions, progressive evolutionary changes, and different dynamic regimes, *Rev. Geophys.,* **46**(4), RG4006, doi:10.1029/2008RG000260.

Ben-Zion, Y., 2019. A critical data gap in earthquake physics, *Seismol. Res. Lett.,* **90,** 1721–1722. doi: 10.1785/0220190167

Ben-Zion, Y. & Ampuero, J.-P., 2009. Seismic radiation from regions sustaining material damage, *Geophys. J. Int.,* **178,** 1351–1356.

Ben-Zion, Y., Dahmen, K., Lyakhovsky, V., Ertas, D. & Agnon, A., 1999. Self-driven mode switching of earthquake activity on a fault system, *Earth planet. Sci. Lett.,* **172**(1–2), 11–21.

Ben-Zion, Y. & Lyakhovsky, V., 2002. Accelerated seismic release and related aspects of seismicity patterns on earthquake faults, *Pure appl. Geophys.,* **159,** 2385–2412.

Ben-Zion, Y. & Lyakhovsky, V., 2006. Analysis of aftershocks in a lithospheric model with seismogenic zone governed by damage rheology, *Geophys. J. Int.,* **165,** 197–210.

Ben-Zion, Y. & Sammis, C.G., 2003. Characterization of fault zones, *Pure appl. Geophys.,* **160,** 677–715.

Ben-Zion, Y. & Zaliapin, I., 2019. Spatial variations of rock damage production by earthquakes in southern California, *Earth planet. Sci. Lett.,* **512,** 184–193.

Bilham, R., 2009. The seismic future of cities, *Bull. Earthq. Eng.,* **7**(4), 839–887.

Breiman, L., Friedman, J., Stone, C.J. & Olshen, R.A., 1984. *Classification and Regression Trees,* CRC Press, pp. 368.

Brenguier, F. *et al.*, 2019. Turning vehicle traffic into a powerful seismic source for monitoring active faults, *Geophys. Res. Lett.,* **46,** 9529–9536.

Brinkman, B.A.W., LeBlanc, M., Ben-Zion, Y., Uhl, J.T. & Dahmen, K.A., 2015. Probing failure susceptibilities of earthquake faults using small-quake tidal correlations, *Nat. Commun.,* **6,** 6157, doi:10.1038/ncomms7157.

Bufe, C.G. & Varnes, D.J., 1993. Predictive modeling of the seismic cycle of the great San Francisco bay region, *J. geophys. Res.,* **98,** 9871–9883.

Cheng, Y., Ross, Z.E. & Ben-Zion, Y., 2018. Diverse volumetric faulting patterns in the San Jacinto fault zone, *J. geophys. Res.,* **123,** 5068–5081.

Chester, F.M., Evans, J.P. & Biegel, R.L., 1993. Internal structure and weakening mechanisms of the San Andreas fault, *J. geophys. Res,* **98,** 771–786.

Craig, T.J., Chanard, K. & Calais, E., 2017. Hydrologically-driven crustal stresses and seismicity in the New Madrid seismic zone, *Nat. Commun.,* **8**(1), 2143.

Dahmen, K., Ertas, D. & Ben-Zion, Y., 1998. Gutenberg richter and characteristic earthquake behavior in simple mean-field models of heterogeneous faults, *Phys. Rev. E,* **58,** 1494–1501.

Davidsen, J., Kwiatek, G., Charalampidou, E.M., Goebel, T., Stanchits, S., Rück, M. & Dresen, G., 2017. Triggering processes in rock fracture, *Phys. Rev. Lett.,* **119**(6), 068501.

Detweiler, S.T. & Wein, A.M. eds., 2017. The HayWired earthquake scenario: U.S. Geological Survey Scientific Investigations Report 2017–5013, doi:10.3133/sir20175013.

Dieterich, J.H. & Kilgore, B.D., 1996. Imaging surface contacts; power law contact distributions and contact stresses in quarts, calcite, glass, and acrylic plastic, *Tectonophysics,* **256,** 219–239.

Dolan, J.F., Bowman, D.D. & Sammis, C.G., 2007. Long-range and long-term fault interactions in Southern California, *Geology,* **35**(9), 855–858.

Eshelby, J.D., 1957. The determination of the elastic field of an ellipsoidal inclusion and related problems, *Proc. R. Soc. Lond., A,* **241,** 376–396.

Field, E.H., Working Group on California Earthquake Probabilities, 2018. Improving earthquake rupture forecasts using California as a Guide, *Seism. Res. Lett.,* **89**(6), 2337–2346.

Finzi, Y., Hearn, E.H., Ben-Zion, Y. & Lyakhovsky, V., 2009. Structural properties and deformation patterns of evolving strike-slip faults: Numerical simulations incorporating damage rheology, *Pure appl. Geophys.,* **166,** 1537–1573.

Fletcher, J.M. *et al.*, 2014. Assembly of a large earthquake from a complex fault system: surface rupture kinematics of the 4 April 2010 El Mayor-Cucapah (Mexico) Mw 7.2 earthquake, *Geosphere,* **10,** 797–827.

Goebel, T.H.W., Becker, T.W., Sammis, C.G., Dresen, G. & Schorlemmer, D., 2014. Off-fault damage and acoustic emission distributions during the evolution of structurally complex faults over series of stick-slip events, *Geophys. J. Int.,* **197**(3), 1705–1718.

Hauksson, E., Yang, W. & Shearer, P.M., 2012. Waveform relocated earthquake catalog for southern California (1981 to June 2011), *Bull. seism. Soc. Am.,* **102**(5), 2239–2244.

Johnson, A.M., Fleming, R.W., Cruikshank, K.M., Martosudarmo, S.Y., Johnson, N.A, Johnson, K.M. & Wei, W., 1997. Analecta of structures

formed during the 28 June 1992 Landers-Big Bear, California earthquake sequence, USGS Open-File Report 97-94.

Johnson, P.A. & Jia, X., 2005. Nonlinear dynamics, granular media and dynamic earthquake triggering, *Nature,* **473,** 871–874.

Jolliffe, I.T. & Stephenson, D.B.eds., 2012. *Forecast Verification: A Practitioner'S Guide in Atmospheric Science,* John Wiley & Sons.

Jordan, T.H. *et al.*, 2011. Operational earthquake forecasting: State of knowledge and guidelines for implementation, Final Report of the International Commission on Earthquake Forecasting for Civil Protection, *Ann. Geophys.,* **54**(4), 315–391. doi: 10.4401/ag-5350

Keilis-Borok, V., 2002. Earthquake prediction: state-of-the-art and emerging possibilities, *Annu. Rev. Earth Planet. Sci.,* **30**(1), 1–33.

Keilis-Borok, V.I. & Kossobokov, V.G., 1990. Premonitory activation of earthquake flow: algorithm M8, *Phys. Earth planet. Inter.,* **61,** 73–83.

Keilis-Borok, V.I. & Soloviev, A.A., 2003. *Nonlinear Dynamics of the Lithosphere and Earthquake Prediction,* Springer Series in Synergetics.

Kreemer, C., Hammond, W.C. & Blewitt, G., 2018. A robust estimation of the 3-D intraplate deformation of the North American plate from GPS, *J. geophys. Res.,* **123** (5), 4388–4412.

Kreemer, C., Blewitt, G. & Klein, E.C., 2014. A geodetic plate motion and global strain rate model. *Geochem. Geophys. Geosyst.,* **15**(10), 3849–3889.

Kurzon, I., Lyakhovsky, V. & Ben-Zion, Y., 2019. Dynamic rupture and seismic radiation in a damage-breakage rheology model, *Pure appl. Geophys.,* **176,** 1003–1020.

Lockner, D.A. & Byerlee, J.D., 1995. Precursory AE patterns leading to rock fracture, in *Proceedings, Fifth Conference on Acoustic Emission/Microseismic Activity in Geological Structures and Materials,* pp. 45–58, ed. Hardy, H.R., Trans Tech Publications, Clausthal-Zellerfeld.

Lockner, D., Byerlee J, D., Kuksenko, V., Ponomarev, A. & Sidorin, A., 1991. Quasi-static fault growth and shear fracture energy in granite, *Nature,* **350,** 39–42.

Lyakhovsky, V. & Ben-Zion, Y., 2009. Evolving geometrical and material properties of fault zones in a damage rheology model, *Geochem. Geophys. Geosyst.,* **10,** Q11011, doi:10.1029/2009GC002543.

Lyakhovsky, V., Ben-Zion, Y. & Agnon, A., 1997. Distributed damage, faulting, and friction, *J. geophys. Res.,* **102,** 27635–27649.

Lyakhovsky, V., Ben-Zion, Y. & Agnon, A., 2001. Earthquake cycle, fault zones, and seismicity patterns in a rheologically layered lithosphere, *J. geophys. Res.,* **106,** 4103–4120.

Lyakhovsky, V., Hamiel, Y. & Ben-Zion, Y., 2011. A non-local visco-elastic damage model and dynamic fracturing, *J. Mech. Phys. Solids,* **59,** 1752–1776.

McBeck, J.A., Cooke, M.L., Herbert, J.W., Maillot, B. & Souloumiac, P., 2017. Work optimization predicts accretionary faulting: an integration of physical and numerical experiments, *J. geophys. Res.,* **122**(9), 7485–7505.

McBeck, J.A., Cordonnier, B., Vinciguerra, S. & Renard, F., 2019. Volumetric and shear strain localization in Mt. Etna basalt, *Geophys. Res. Lett.,* **46**(5), 2425–2433.

Mignan, A., Bowman, D.D. & King, G.C.P., 2006. An observational test of the origin of accelerating moment release before large earthquakes, *J. geophys. Res.,* **111,** B11304, doi:10.1029/2006JB004374.

Milliner, C.W.D., Dolan, J.F., Hollingsworth, J., Leprince, S., Ayoub, F. & Sammis, C.G., 2015. Quantifying near-field and off-fault deformation patterns of the 1992 Mw7.3 Landers earthquake, *Geochem. Geophys. Geosyst.,* **16,** 1577–1598.

Mogi, K., 1969. Some features of recent seismic activity in and near Japan(2), activity before and after great earthquakes, *Bull. Earthq. Res. Inst. Univ. Tokyo,* **47,** 395–417.

Molchan, G. & Keilis-Borok, V., 2008. Earthquake prediction: probabilistic aspect. *Geophys. J. Int.,* **173**(3), 1012–1017.

Nakatani, M. & Scholz, C.H., 2004. Frictional healing of quartz gouge under hydrothermal conditions: 1. Experimental evidence for solution transfer healing mechanism, *J. geophys. Res.,* **109,** B07201, doi:10.1029/2001JB001522.

Niu, F., Silver, P.G., Daley, T.M., Cheng, X. & Majer, E.L., 2008. Preseismic velocity changes observed from active source monitoring at the Parkfield SAFOD drill site, *Nature,* **454**(7201), 204–208.

Pei, S., Niu, F., Ben-Zion, Y., Sun, Q., Liu, Y., Xue, X., Su, J. & Shao, Z., 2019. Seismic velocity reduction and accelerated recovery due to earthquakes on the Longmenshan fault, *Nature Geosci.,* **12,** 387–392.

Peng, Z., Hill, D.P., Shelly, D.R. & Aiken, C., 2010. Remotely triggered microearthquakes and tremor in Central California following the 2010 Mw8.8 Chile Earthquake, *Geophys. Res. Lett.,* **37,** L24312, doi:10.1029/2010GL045462.

Paterson, M.S. & Wong, T.F., 2005. Experimental rock deformation-the brittle field. Springer Science & Business Media., 348, Springer Science & Business Media, Heidelberg, New York.

Petersen, M.D., Moschetti, M.P., Powers, P.M., Mueller, C.S., Haller, K.M., Frankel, A.D. & Olsen, A.H., 2014, *Documentation for the 2014 Update of the United States National Seismic Hazard Maps, USGS Open-File report 201–1091.*

Reches, Z., 1988. Evolution of fault patterns in clay experiments, *Tectonophysics,* **145,** 141–156.

Reches, Z.E. & Lockner, D.A., 1994. Nucleation and growth of faults in brittle rocks, *J. geophys. Res.,* **99**(B9), 18159–18 173.

Renard, F., Weiss, J., Mathiesen, J., Ben Zion, Y., Kandula, N. & Cordonnier, B., 2018. Critical evolution of damage towards system-size failure in crystalline rock, *J. Geophys. Res,* **123,** 1969–1986. doi: 10.1002/2017JB014964.

Renard, F., McBeck, J., Kandula, N., Cordonnier, B., Meakin, P. & Ben-Zion, Y., 2019. Volumetric and shear processes in crystalline rock on the approach to faulting, *Proc. Natl. Acad. Sci. U.S.A.,* **116,** 16 234–16 239.

Rhoades, D.A. & Evison, F.F., 2004. Long-range earthquake forecasting with every earthquake a precursor according to scale, *Pure appl. Geophys.,* **161,** 47–71.

Rhoades, D.A. & Evison, F.F., 2005. Test of the EEPAS forecasting model on the Japan Earthquake Catalogue, *Pure appl. Geophys.,* **162,** 1271–1290.

Rockwell, T.K. & Ben-Zion, Y., 2007. High localization of primary slip zones in large earthquakes from paleoseismic trenches: observations and implications for earthquake physics, *J. geophys. Res.,* **112,** B10304, doi:10.1029/2006JB004764.

Rockwell, T.K., Dawson, T.E., Young-Ben Horton, J. & Seitz, G., 2015. A 21 event, 4,000-year history of surface ruptures in the Anza Seismic Gap, San Jacinto Fault and implications for long-term earthquake production on a major plate boundary fault, *Pure appl. Geophys.,* **172**(5), 1143–1165.

Ross, Z.E., Ben-Zion, Y., White, M.C. & Vernon, F.L., 2016. Analysis of earthquake body wave spectra for potency and magnitude values: implications for magnitude scaling relations, *Geophys. J. Int,* **207,** 1158–1164.

Schaff, D.P. & Waldhauser, F., 2005. Waveform cross-correlation-based differential travel-time measurements at the Northern California Seismic Network, *Bull. seism. Soc. Am.,* **95,** 2446–2461.

Schulte-Pelkum, V., Ross, Z.E., Mueller, K. & Ben-Zion, Y., 2020. Tectonic inheritance from deformation fabric in the brittle and ductile southern California crust, *J. geophys. Res. Solid Earth,* e2020JB019525. doi: 10.1029/2020JB019525.

Seeber, L., Armbruster, J.G., Ozer, N., Aktar, M., Baris, S., Okaya, D., Ben-Zion, Y. & Field, E., 2000. The 1999 earthquake sequence along the North Anatolia transform at the juncture between the two main ruptures, in *The 1999 Izmit and Duzce Earthquakes: Preliminary Results,* eds Barka, A., Kazaci, O., Akyuz, S. & Altunel, E., Istanbul Technical University, pp. 209–223.

Shannon, C.E., 1948. A mathematical theory of communication. *Bell Syst. Tech. J.,* **27**(3), 379–423.

Shcherbakov, R., Turcotte, D.L., Rundle, J.B., Tiampo, K.F. & Holliday, J.R., 2010. Forecasting the locations of future large earthquakes: an analysis and verification. *Pure appl. Geophys.,* **167**(6–7), 743–749.

Shen, Z.K., Wang, M., Zeng, Y. & Wang, F., 2015. Optimal interpolation of spatially discretized geodetic data. *Bull. seism. Soc. Am.,* **105**(4), 2117–2127.

Socquet, A. *et al.*, 2017. An 8 month slow slip event triggers progressive nucleation of the 2014 Chile megathrust, *Geophys. Res. Lett.,* **44,** doi:10.1002/2017GL073023.

Stanchits, S., Vinciguerra, S. & Dresen, G., 2006. Ultrasonic velocities, acoustic emission characteristics and crack damage of basalt and granite, *Pure appl. Geophys.,* **163,** 974–993.

Swets, J.A., 1973. The relative operating characteristic in psychology: a technique for isolating effects of response bias finds wide use in the study of perception and cognition. *Science,* **182**(4116), 990–1000.

Tanaka, S., 2012. Tidal triggering of earthquakes prior to the 2011 Tohoku-Oki earthquake (Mw 9.1), *Geophys. Res. Lett.,* **39,** L00G26, doi:10.1029/2012GL051179.

Thurber, C., Zhang, H., Waldhauser, F., Hardebeck, J., Michael, A. & Eberhart-Phillips, D., 2006. Three-dimensional compressional wavespeed model, earthquake relocations, and focal mechanisms for the Parkfield, California, region, *Bull. seism. Soc. Am.,* **96**(4B), S38–S49.

Turcotte, D.L., 1997. *Fractals and Chaos in Geology and Geophysics,* Cambridge Univ. Press.

Waldhauser, F. & Schaff, D.P., 2008. Large-scale relocation of two decades of Northern California seismicity using cross-correlation and double-difference methods, *J. geophys. Res.,* **113,** B08311, doi:10.1029/2007JB005479.

Wdowinski, S., Sudman, Y. & Bock, Y., 2001. Geodetic detection of active faults in S. California. *Geophys. Res. Lett.,* **28**(12), 2321–2324.

Wu, C., Peng, Z. & Ben-Zion, Y., 2009. Non-linearity and temporal changes of fault zone site response associated with strong ground motion, *Geophys. J. Int.,* **176,** 265–278.

Yu, W.C., Song, T.R.A. & Silver, P.G., 2013. Temporal velocity changes in the crust associated with the Great Sumatra earthquakes, *Bull. seism. Soc. Am.,* **103**(5), 2797–2809.

Zaliapin, I. & Ben-Zion, Y., 2013. Earthquake clusters in southern California. I: identification and stability, *J. geophys. Res.,* **118**(6), 2847–2864. doi:10.1002/jgrb.50179

Zaliapin, I. & Ben-Zion, Y., 2015. Artefacts of earthquake location errors and short-term incompleteness on seismicity clusters in southern California, *Geophys. J. Int.,* **202**(3), 1949–1968.

Zaliapin, I. & Ben-Zion, Y., 2016. Discriminating characteristics of tectonic and human-induced seismicity, *Bulletin of the Seismol. Soc. Am.,* **106**(3), pp.846–859.

Zaliapin, I. & Ben-Zion, Y., 2018. Localization processes leading to large failures: analysis of acoustic emission and earthquake catalogs. Abstract of the *Banff 2018 International Induced Seismicity Workshop*, 24–27 October 2018, Banff, Canada.

Zaliapin, I. & Ben-Zion, Y., 2020. Earthquake declustering using the nearest-neighbor approach in space-time-magnitude domain, *J. geophys. Res.,* **125,** e2018JB017120, doi:10.1029/2018JB017120.

Zaliapin, I., Gabrielov, A., Keilis-Borok, V. & Wong, H., 2008. Clustering analysis of seismicity and aftershock identification, *Phys. Rev. Lett.,* **101**(1), p.018501. DOI:10.1103/PhysRevLett.101.018501.

Zeng, Y., Petersen, M.D. & Shen, Z.-K., 2018. Earthquake potential in California-Nevada implied by correlation of strain rate and seismicity, *Geophys. Res. Lett.,* **45,** 1778–1785.

SUPPORTING INFORMATION

Supplementary data are available at *GJI* online.

Figure S1. Horizontal location errors in km, averaged over background events with $M \geq 3.0$ within a sliding time window of 10 yr. Different colours correspond to different regions: Entire Southern California (blue), Eastern Southern California (red), San Jacinto & Elsinore fault zones (black) and Mountains & Basins (green).

Figure S2. Absolute long-term localization $G_{S(t)}$ of background events. Red—observations, black—reshuffled catalogues with simulated 95 per cent confidence interval. (a) Entire Southern California. (b) Eastern Southern California. (c) San Jacinto and Elsinore fault zones. (d) Mountains and Basins. The analysis parameters are reported in Table 1.

Figure S3. Relative long-term localization $G_{S(t)|S}$ of background events. Red—observations, black—reshuffled catalogues with simulated 95 per cent confidence interval. (a) Entire Southern California. (b) Eastern Southern California. (c) San Jacinto and Elsinore fault zones. (d) Mountains and Basins. The analysis parameters are reported in Table 1.

Figure S4. Long-term localization of background events—ROC set $R(S(t)|U, S(t))$. Different colours correspond to different time windows (see colourbar). (a) Entire Southern California. (b) Eastern Southern California. (c) San Jacinto and Elsinore fault zones. (d) Mountains and Basins. Table 1 lists the analysis parameters.

Figure S5. Localization of background events before large earthquakes—normalized proportion $P[S(t)]$ of occupied cells. Red—observations, black—reshuffled catalogues (with simulated 95 per cent confidence interval). (a) Landers, $M7.3$. (b) El Mayor-Cucapah, $M7.2$. (c) Ridgecrest, $M7.1$. (d) Parkfield, $M6$. Note the opposite trend (delocalization) prior to the $M6$ Parkfield event. Table 1 lists the analysis parameters.

Figure S6. Relative localization $G_{S(t)|S}$ of background events before large earthquakes. Red—observations, black—reshuffled catalogues (with simulated 95 per cent confidence interval). (a) Landers, $M7.3$. (b) El Mayor-Cucapah, $M7.2$. (c) Ridgecrest, $M7.1$. (d) Parkfield, $M6$. Note the opposite trend (delocalization) prior to Parkfield. Table 1 lists the analysis parameters.

Figure S7. Map of seismicity examined for localization of background events prior to the 1999 $M7.2$ Düzce earthquake. The analysis parameters are listed in Table 1.

Figure S8. Localization of background events before the 1999 $M7.2$ Düzce earthquake. Red—observations, black—reshuffled catalogues (with simulated 95 per cent confidence interval). (a) Normalized proportion $P[S(t)]$ of occupied cells. (b) Absolute localization $G_{S(t)}$. (c) Relative localization $G_{S(t)|S}$. Table 1 lists the analysis parameters.

Figure S9. Localization of background events before the 1999 $M7.2$ Düzce earthquake—ROC set $R(S(t)|U, S(t))$. Different colours correspond to different time windows (see colourbar). Table 1 lists the analysis parameters.

Figure S10. Evolving earthquake clustering before the 1999 $M7.2$ Düzce earthquake. Black line shows the average cluster size in sliding time windows and the vertical red line on the right marks the time of the main shock. Green horizontal dashed line emphasizes changes of the average cluster size prior to the main shock. Table 2 lists the analysis parameters.

Please note: Oxford University Press is not responsible for the content or functionality of any supporting materials supplied by the authors. Any queries (other than missing material) should be directed to the corresponding author for the paper.

APPENDIX A: CONDITIONAL RECEIVER OPERATING CHARACTERISTIC (ROC)

The conditional ROC of a probability measure (e.g. Swets 1973; Molchan & Keilis-Borok 2008; Shcherbakov *et al.* 2010; Jolliffe & Stephenson 2012) is a key tool of our localization analysis. Here we only use discrete measures, which simplify the setup, but similar results can be obtained also for continuous measures. Consider a set X (which can be multidimensional) partitioned into a finite collection of m non-overlapping subsets
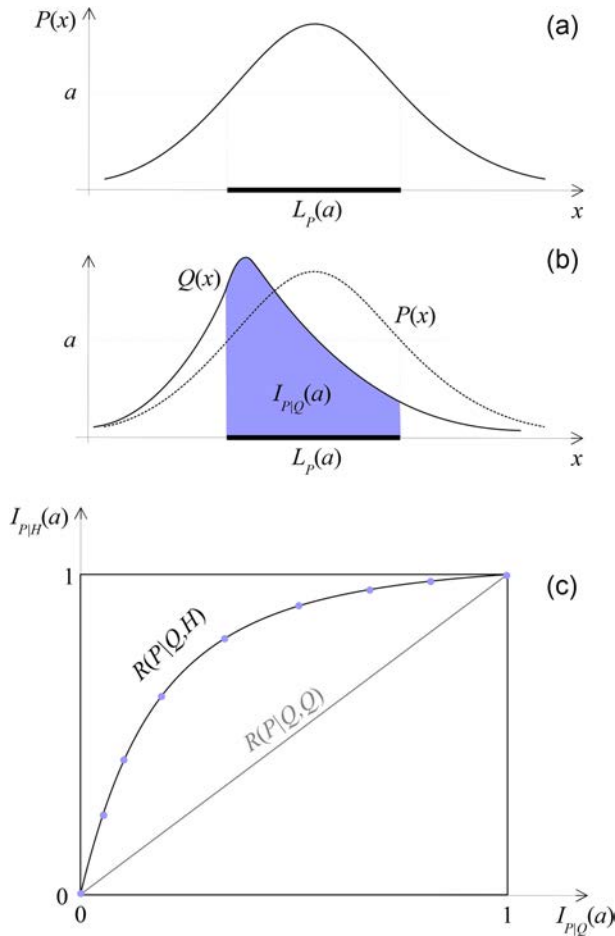
$$X = \{X_i, i = 1, \ldots, m\}. \tag{A1}$$

Figure A1. ROC analysis: illustration for measures on the real line. (a) Level set $L_P(a)$ of measure $P(x)$ is a real interval (in general—collection of intervals). (b) Mass $I_{P|Q}(a)$ of the level set $L_P(a)$ with respect to measure $Q(x)$ equals the area of the shaded region. Measure $P(x)$ is shown by dashed line. (c) ROC diagram $R(P|Q,H)$: a parametric plot of $I_{P|H}(a)$ vs $I_{P|Q}(a)$ for $a \geq 0$. The set $R(P|Q,Q)$ always lies on the diagonal (grey).

A measure P on X is a non-negative additive function on these subsets and their unions, so that $P(X_i) \geq 0$ and $P(X_i) + P(X_j) = P(X_i \cup X_j)$. We define upper level set $L_P(a)$ of measure P (Fig. A1a) to be

$$L_P(a) = \{X_i : P(X_i) \geq a\} \text{ for any non-negative } a. \qquad (A2)$$

The proposed methodology is based on measuring the level sets of one measure with respect to another measure. Specifically, for any pair of measures P and Q, the measure of the level set $L_P(a)$ with respect to Q is denoted by $I_{P|Q}(a)$ and defined (Fig. A1b) as

$$I_{P|Q}(a) = \sum_{X_i \subset L_P(a)} Q(X_i). \qquad (A3)$$

Consider now three measures P, Q and H on the same set X. Any pair of measures (or all of them) may coincide. The conditional receiver operating characteristic of measure P with respect to the ordered pair of measures Q and H, denoted by $R(P|Q,H)$, is the 2-D parametric set $(I_{P|Q}(a), I_{P|H}(a))$ with parameter $a \geq 0$ (Fig. A1c). In words, every point in the set $R(P|Q,H)$ corresponds to a particular level set $L_P(a)$. The x and y coordinates

of the point equal the measure of the level set $L_P(a)$ according to the measures Q and H, respectively. In this work, we use normalized (probability) measures that satisfy $P(X) = Q(X) = H(X) = 1$. This definition then implies the following properties (Fig. A1c):

(1) The set $R(P|Q,H)$ is contained within the unit square $[0,1] \times [0,1]$.

(2) The set $R(P|Q,H)$ includes the points $(I_{P|Q}(\infty), I_{P|H}(\infty)) = (0,0)$ and $(I_{P|Q}(0), I_{P|H}(0)) = (1,1)$.

(3) The set $R(P|Q,H)$ consists of a finite number of points; the number of points is one more than the number of distinct values of $P(X_i)$, $i = 1, \ldots, m$.

(4) The set $R(P|Q,H)$ is monotone non-decreasing: $I_{P|Q}(a) < I_{P|Q}(b)$ implies $I_{P|H}(a) \leq I_{P|H}(b)$ for any non-negative pair a, b.

(5) For any pair of measures P and Q, the set $R(P|Q,Q)$ lies on the diagonal line between the points $(0,0)$ and $(1,1)$.

(6) For the uniform measure U that assigns the same value to each subset X_i, and any pair of measures Q and H, the set $R(U|Q,H)$ consists of the two points: $(0,0)$ and $(1,1)$.

A1 Quantifying absolute localization of a measure

The ROC diagram is a useful tool to compare measures on the same domain and to quantify the degree of localization (concentration) of a given measure. Toward this goal, we notice the following property:

(1) For any measure P and the uniform measure U, the set $R(P|U,P)$ lies on or above the diagonal line between the points $(0,0)$ and $(1,1)$. Moreover, the set $R(P|U,P)$ contains at least one point above the diagonal line, unless $P = U$.

This property is explained by inhomogeneities in P—existence of subsets X_i with higher measure than in other subsets. This results in accumulation of a higher value over the level sets of P when integrated with respect to P itself rather than with respect to U. The amount of deviation of $R(P|U,P)$ from the diagonal line may serve as a measure of absolute localization of P. Indeed, if there exists a level set L such that $P(L) = y$ and $U(L) = x$, then the set $R(P|U,P)$ contains the point (x,y). Concentration of a large fraction of P within a small region L results in the point (x,y) being located close to the corner point $(0,1)$, far from the diagonal line.

We use here a particular measure of absolute localization—twice the area between the convex envelop of $R(P|U,P)$ and the diagonal line, known as the Gini coefficient (Breiman *et al.* 1984) and denoted by G_P (Fig. A2a). The coefficient G_P assumes values within the interval $[0,1)$; $G_P = 0$ implies $P = U$, and G_P increases toward unity when P becomes more inhomogeneous (more localized). The Gini coefficient can be made as close to unity as desired, by constructing a measure that is completely concentrated in one of the m subsets of X. This corresponds to the point $(m^{-1}, 1)$ on the ROC diagram. Fig. A3(a) shows three measures with different levels of absolute localization; their ROC diagrams and Gini coefficients are illustrated in Fig. A3(b).

A2 Quantifying relative localization of a measure

The absolute localization of Appendix A1 compares a measure P with the uniform measure U on the same support. It is also important to examine *relative* localization of a measure P with respect to another non-uniform measure Q. Informally, the relative localization means that measure P concentrates within the
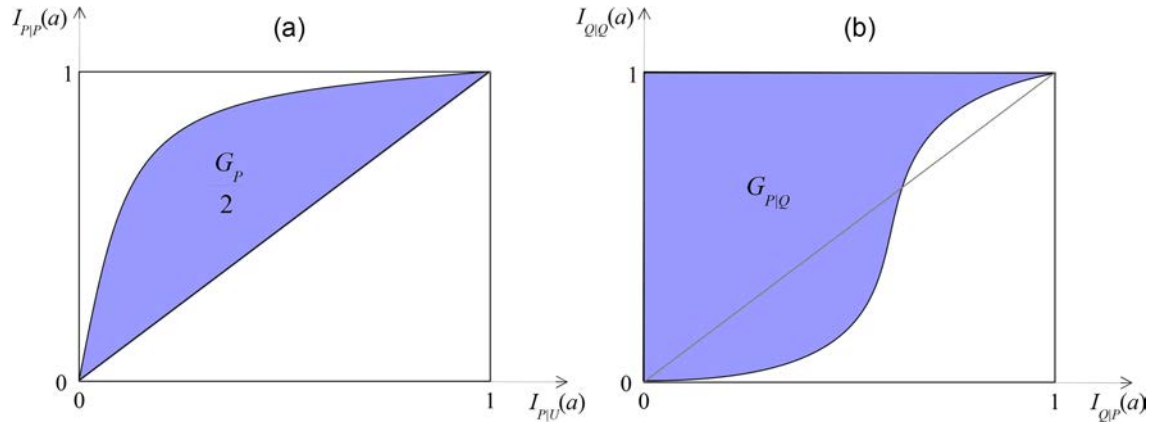
Figure A2. Statistics used to quantify localization of measure $P(x)$. (a) Absolute localization of $P(x)$ is quantified by the Gini coefficient G_P (twice the shaded area) calculated for the set $R(P|U,P)$, which is shown by the curve above the diagonal. (b) Relative localization of $P(x)$ with respect to measure $Q(x)$ is quantified by the coefficient $G_{P|Q}$ (the shaded area) calculated for the set $R(Q|P,Q)$, which is shown by the curve that wanders about the diagonal.

same domain as Q and is more localized in the absolute sense of Appendix A1 (i.e. has more pronounced peaks). This concept is illustrated Figs A3(c) and (e). Here, panel (c) shows two measures, P (blue) and Q (red), that are concentrated within different areas—this is *not* relative concentration, despite the fact that P has larger absolute localization (higher Gini coefficient) than Q. Panel (e) shows two measures such that P (blue) is a localized version of Q (red). In this panel, not only P (blue) has larger absolute concentration than Q (red), but also it is located within the same domain. Our goal is to quantify this effect. A naïve substitution of Q in place of U in the absolute localization framework of Appendix A1 is not useful, since a non-zero value of the Gini coefficient for the set $R(P|Q,P)$ may simply reflect the fact that measures P and Q are concentrated within different subdomains of X. This situation is illustrated in Figs A3(c) and (d).

To focus on the *relative* localization, we consider the set $R(Q|P,Q)$ that operates with the level sets of measure Q. This set may include points below the diagonal line; such points indicate that the corresponding level sets of measure Q accumulate a higher mass with respect to measure P than with respect to Q itself. We interpret this as relative localization of P with respect to Q. This situation is illustrated in Figs A3(e) and (f). In panel (e), the measure P (blue) is a localized version of measure Q (red). This relative localization places the set $R(Q|P,Q)$, which operates with level sets of $Q(x)$, below the diagonal. Notice also that the set $R(P|Q,P)$, which operates with the level sets of $P(x)$, is above the diagonal and does not reflect the information about relative localization (*cf.* panels c and d). Hence, we quantify the relative localization of a measure P with respect to a measure Q by the area above the convex envelop of $R(Q|P,Q)$, this parameter is denoted $G_{P|Q}$ (Fig. A2b). The parameter $G_{P|Q}$ assumes values within the interval $(0, 1)$. If measures P and Q are concentrated within different regions, then $G_{P|Q} < 1/2$ (Figs A3c and d); $P = Q$ implies $G_{P|Q} = 1/2$ (but not vice versa, since $R(Q|P,Q)$ may cross the diagonal); and localization of P with respect to Q implies $G_{P|Q} > 1/2$ (Figs A3e and f).
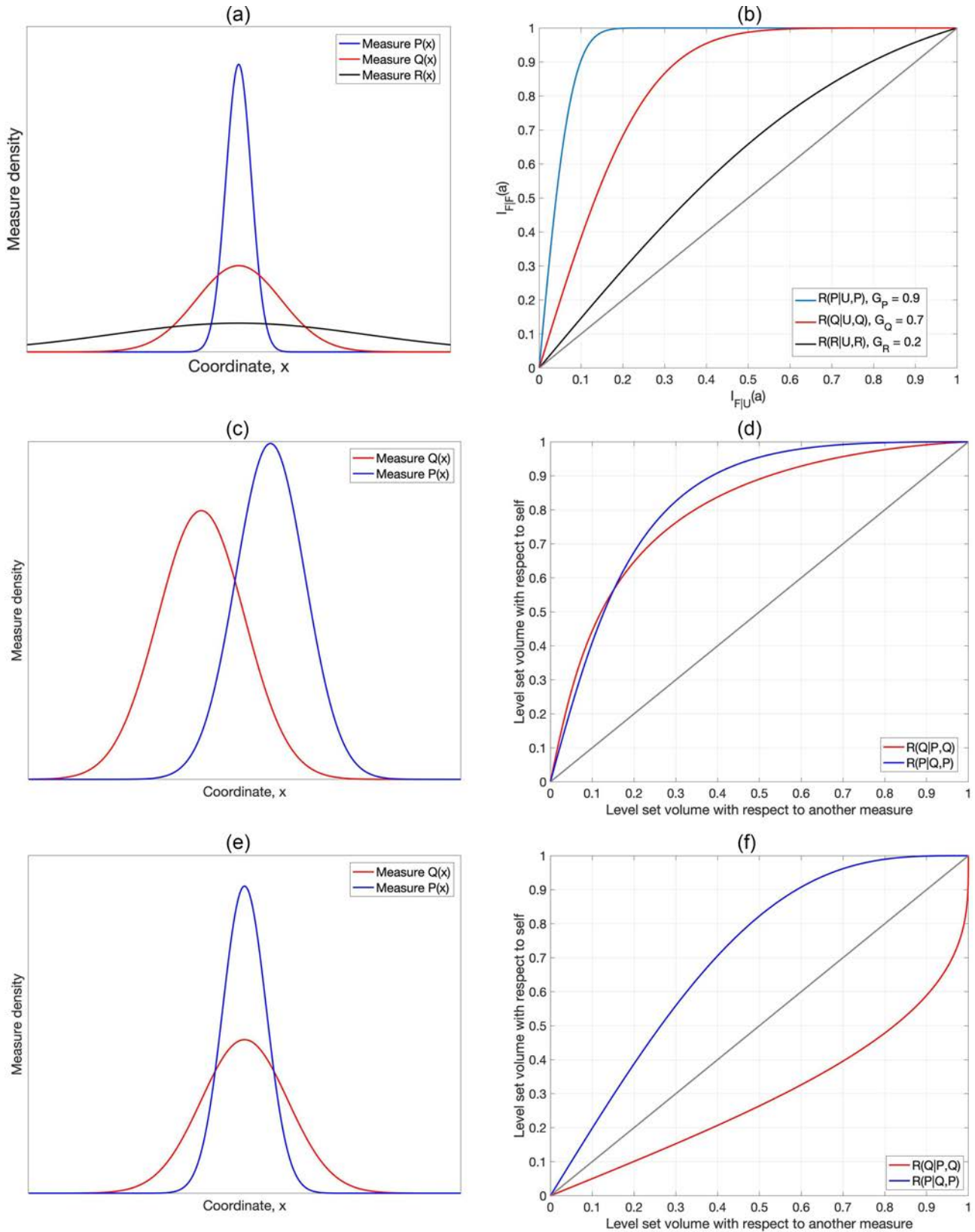
Figure A3. Localization metrics: an illustration. (a) Three measures with different levels of absolute localization (blue is the most localized). (b) ROC sets $R(\cdot|U, \cdot)$ for the measures of panel (a) and their Gini coefficients. The axis labels use generic name F for an examined measure, which can be one of P, Q, R. (c) Measures $P(x)$ and $Q(x)$ concentrated within different regions. (d) ROC sets $R(P|Q,P)$ and $R(Q|P,Q)$ for the measures of panel (c). Note that both sets are located above the diagonal line. (e) Measure $P(x)$ (blue) is a localized version of measure $Q(x)$ (red). (f) ROC sets $R(P|Q,P)$ and $R(Q|P,Q)$ for the measures of panel (e). Note that $R(Q|P,Q)$ is below the diagonal line.

APPENDIX B: NEAREST-NEIGHBOUR EARTHQUAKE PROXIMITY

We use a simplified version of the nearest-neighbour earthquake proximity to examine the development of earthquake clustering (Sections 3.3 and 4.6). The proximity is defined below, closely following Baiesi & Paczuski (2004), Zaliapin *et al.* (2008) and Zaliapin & Ben-Zion (2013, 2020). We refer to these works for further details and references regarding the applications of this proximity in analyses of earthquake catalogues and acoustic emission experiments.

Consider a catalogue of earthquakes where each event i is characterized by its occurrence time t_i, hypocentre $\mathbf{x}_i = (\phi_i, \lambda_i, z_i)$ and magnitude M_i. The proximity of earthquake j to previous earthquake i is asymmetric in time and is defined as

$$\eta_{ij} = \begin{cases} t_{ij} \left(r_{ij} \right)^d 10^{-wM_i}, & t_{ij} > 0; \\ \infty, & t_{ij} \leq 0. \end{cases} \quad \text{(B1)}$$

Here, $t_{ij} = t_j - t_i$ is the event intercurrence time, which is positive if event j occurred after event i; $r_{ij} \geq 0$ is the spatial distance between the earthquake hypocentres (or epicentres); d is the fractal dimension of the hypocentres (or epicentres); and w is the parameter that introduces exponential weight of the earlier event i by its magnitude. In cluster analyses, this parameter usually equals the b-value of the Gutenberg–Richter law that approximates the observed number $N(m)$ of events with magnitude above m:

$$\log_{10} N(m) = a - bm, \quad b \approx 1, \quad m \geq m_c. \quad \text{(B2)}$$

In this study, we work with epicentres of events.

Intuitively, the earthquake proximity (B1) is the expected number of events within the space–time region 'between' the examined pair of earthquakes in a stationary marked point process with independent space and time components and exponential magnitudes; see Zaliapin & Ben-Zion (2016, eq. 4) for further discussion.